9-18-2018

Paleointensity Estimates From Ignimbrites: The Bishop Tuff Revisited

Margaret S. Avery
University of California - Berkeley, msavery@berkeley.edu

Jeffrey S. Gee
University of California - San Diego, jsgee@ucsd.edu

Julie A. Bowles
University of Wisconsin-Milwaukee, bowlesj@uwm.edu

Recommended Citation

Avery, M. S., Gee, J. S., Bowles, J. A., & Jackson, M. J. (2018). Paleointensity estimates from ignimbrites: The Bishop Tuff revisited. Geochemistry, Geophysics, Geosystems, 19, 3811–3831. https://doi.org/10.1029/2018GC007665

AGU100 ADVANCING EARTH AND SPACE SCIENCE

Geochemistry, Geophysics, Geosystems

RESEARCH ARTICLE
10.1029/2018GC007665

Key Points:
- Large pyroclastic flows may be unsuitably complex for paleointensity studies. Extreme caution is required
- Hydrothermal alteration has large impact on paleointensity estimates
- Thermochemical remanent magnetizations may not be rejected by paleointensity experimental selection criteria

Supporting Information:
- Supporting Information S1
- Figure S1
- Figure S2
- Figure S3
- Figure S4
- Table S1
- Table S2

Correspondence to:
M. S. Avery,
msavery@berkeley.edu

Citation:
Avery, M. S., Gee, J. S., Bowles, J. A., & Jackson, M. J. (2018). Paleointensity estimates from ignimbrites: The Bishop Tuff revisited. *Geochemistry, Geophysics, Geosystems*, *19*, 3811–3831. https://doi.org/10.1029/2018GC007665

Received 7 MAY 2018
Accepted 23 SEP 2018
Accepted article online 27 SEP 2018
Published online 18 OCT 2018

Paleointensity Estimates From Ignimbrites: The Bishop Tuff Revisited

Margaret S. Avery[1,2], Jeffrey S. Gee[2], Julie A. Bowles[3], and Michael J. Jackson[4]

[1]Earth and Planetary Sciences, University of California, Berkeley, CA, USA, [2]Scripps Institution of Oceanography, University of California - San Diego, La Jolla, CA, USA, [3]Department of Geosciences, University of Wisconsin-Milwaukee, Milwaukee, WI, USA, [4]Institute for Rock Magnetism, Winchell School of Earth Sciences, University of Minnesota, Minneapolis, MN, USA

Abstract Volcanic ash flow tuffs (ignimbrites) may contain single domain-sized (titano) magnetite that should be good for recording geomagnetic field intensity, but due to their complex thermal histories also contain other magnetic grains, which can complicate and obscure paleointensity determination. An initial study of the suitability of the ~767 ka Bishop Tuff for measuring paleointensity found an internally consistent estimate of 43.0 ± 3.2 μT. This initial study also showed a spatial heterogeneity in reliable paleointensity estimates that is possibly associated with vapor-phase alteration and fumarolic activity, which motivated resampling of the Bishop Tuff to examine spatial changes in magnetic properties. Three new stratigraphic sections of the Bishop Tuff within the Owens River gorge were sampled, and the paleointensity results from the initial study in the same locality were reinterpreted. The mean of all sites is 41.9 ± 11.8 μT; this agrees with the initial study's finding but with substantially greater scatter. Two sections show evidence of vapor-phase alteration where the presence of titanohematite, likely carrying a thermochemical remanence, produces nonideal behavior. This thermochemical remanence in the upper portion of the section also produces some paleointensity estimates of technically high quality that have significantly higher intensity than the rest of the tuff. Our best estimate for paleointensity, 39.6 ± 9.9 μT, comes from the densely welded ignimbrite that was emplaced above the Curie temperature of magnetite. The low permeability of this unit likely shielded it from vapor-phase alteration. Our results suggest that care must be taken in interpreting paleointensity data from large tuffs as nonthermal remanence may be present.

Plain Language Summary Understanding past variations of Earth's magnetic field help us understand processes in Earth's core and help us to better understand current field behavior, which is important to life on Earth. Earth's field is recorded by magnetic-minerals in rocks as they form. Variations in the strength of the magnetic field (paleointensity) are less well known than large variations in direction. This is partially due to the difficulty in identifying rocks that are suitable for paleointensity experiments. Rocks made of volcanic ash (ignimbrites) have been shown to successfully record the field strength during recent volcanic eruptions. However, we show evidence that ignimbrites may not all be suitable for paleointensity studies. The Bishop Tuff, located in eastern California, erupted about 767 thousand years ago, emplacing a large volume (~200 km^3, i.e., about 80 million Olympic swimming pools or slightly bigger than Lake Tahoe) of ash and lava over a few days. With samples from the Bishop Tuff we test variations in magnetic-mineralogy that may be related to venting volcanic gas, interaction with water, eruption temperatures, or the degree to which the ash compacted and solidified into rock. These factors affect the magnetic-minerals' ability to record paleointensity and the success rate of our experiments.

1. Introduction

The geomagnetic field varies both temporally and spatially. Learning about its past variations can help us to better understand its current behavior. Additionally, a detailed record of long-term paleomagnetic field variations is needed to reconstruct the evolution of the geodynamo and can provide important information on Earth's thermal history (e.g., Davies & Constable, 2014; Driscoll, 2016; Smirnov et al., 2016). Although the pattern of past reversals of the geomagnetic field is relatively well known, at least for the past 170 Ma, the history of the magnetic field's intensity is not as well constrained, in part because of the difficulty in identifying geological materials that are suitable for paleointensity studies. Volcanic ash flow tuffs (ignimbrites) are potentially useful for fleshing out the spatial and temporal variations of the paleofield, as

they occur throughout the global geologic record and are usually well suited for radiometric dating (e.g., Ickert et al., 2015; Mark et al., 2017; McIntosh et al., 1990; Sarna-Wojcicki et al., 2000; van der Bogaard & Schirnick, 1995).

Portions of some ignimbrites have been shown to contain fine-grained (superparamagnetic [SP] to single domain [SD]) cubic iron oxides preserved in silicic glass (Geissman et al., 1983; Schlinger et al., 1991; Worm & Jackson, 1999). The fine-grained magnetic minerals are thought to crystallize within the flow after emplacement and above the glass transition temperature (typically 550–600 °C for silicic glasses, Giordano et al., 2005), and therefore possibly record a thermoremanent magnetization (TRM). Moreover, this glassy matrix —if fresh—should reduce alteration that often occurs due to exposure to air during the multiple laboratory heatings required to estimate the paleointensity.

Although the fine-grained magnetic particles in silicic glass of tuffs should be suitable for producing accurate absolute paleointensity estimates, there are several factors that can complicate paleointensity studies. Along with possible fine-grained iron oxides within the glassy matrix, tuffs also commonly contain coarser-grained titanomagnetite phenocrysts, which would be multidomain and poor remanence recorders (e.g., Geissman et al., 1983; Hildreth, 1979; Palmer et al., 1996; Reynolds, 1977; Rosenbaum, 1993; Schlinger et al., 1991). Cooling history can also affect the observed Curie temperature (T_C) in some titanomagnetites due to cation reordering (Bowles et al., 2013), which can complicate paleointensity studies (Bowles et al., 2015). Moreover, postemplacement alteration may result in magnetizations that are not pure TRM, but instead are thermochemical remanent magnetization (TCRM; Perrin et al., 2013). In the interiors of cooling thick tuff deposits, water vapor is released during devitrification and is sometimes supplemented with meteoric water, providing a system for redistributing constituents and forming new minerals including magnetic oxides (Vaniman, 2006). Both the possible alteration of primary magnetic minerals and formation of new magnetic oxides below their Curie temperatures result in a chemical or TCRM that may preclude determination of reliable paleointensity estimates. Finally, the magnetic mineralogy, and consequently, the reliability, of paleointensity estimates from tuffs might vary considerably with stratigraphic level, depending on variations in emplacement temperature, cooling history, and postemplacement vapor-phase alteration (Schlinger et al., 1991).

An important test of the reliability of new absolute paleointensity methods or materials is to compare paleointensity estimates from historical flows to the field intensity known from global geomagnetic field models at the time of eruption. Bowles et al. (2015) estimated the paleointensity from historical pyroclastic flows and found two sources of nonideal behavior: unstable remanence of multidomain titanomagnetites due to cation reordering, and nonlinear Arai plots linked to postemplacement alteration leading to underestimates of the paleointensity within alteration zones. The authors rejected samples displaying these behaviors and successfully recovered the historical paleointensity.

Despite the successful recovery of historical field values from recent ignimbrite deposits, there is evidence that ignimbrites may not all be suitable for paleointensity studies without thoroughly examining the nature of the remanence (whether thermal, chemical, or a mixture). Recent studies have sampled ignimbrite of varying density (Gee et al., 2010), sampled whole rock and glass from welded tuffs (Mochizuki et al., 2013), and sampled both extrusive lava and ignimbrite (Perrin et al., 2013) to test the consistency of their paleointensity estimates. Both Mochizuki et al. (2013) and Perrin et al. (2013) observed Arai plots from ignimbrites that passed their selection criteria but which produced inexplicably high or low paleofield estimates. These studies present troubling examples where potentially a chemical remanent magnetization (CRM) or TRCM may produce paleointensity data of high technical quality that nevertheless gives a biased paleointensity estimate if misinterpreted as a TRM.

The pilot study of Gee et al. (2010) determined paleointensity as a function of stratigraphic level in the Bishop Tuff and produced an internally consistent paleofield estimate; however, not all stratigraphic profiles through the tuff produced paleointensity estimates that met the selection criteria (e.g., one of the three sections produced no reliable results). Here we extend the sampling of Gee et al. (2010) to better evaluate the spatial variability of paleofield estimates in the Bishop Tuff. The variable quality of paleointensity results is likely controlled by the thermal history of the tuff, either through variations in emplacement temperature or vapor-phase alteration associated with fumarolic activity. Interestingly, the paleointensity estimate from the Bishop Tuff of Fu et al. (2017), which used single zircon crystal samples, agrees with that of Gee et al. (2010) when they rejected zircon samples with high temperature remanence possibly carried by

maghemite inclusions that gave systematically higher paleointensities. By returning to the large and complex Bishop Tuff, we can test more thoroughly the spatial variations in magnetic mineralogy and magnetization with respect to areas with fossil fumaroles (i.e., vents for volcanic gases), emplacement temperature, and cooling rate, and their effects on the success rate of the modified Thellier-Thellier paleointensity experiment.

The Bishop Tuff is a suitable location to study the reliability of paleointensity estimates because previous studies have documented its eruptive and cooling history (Wilson & Hildreth, 2003), postemplacement alteration (Holt & Taylor, 1998; Sheridan, 1970), and magnetic remanence (Gee et al., 2010; Palmer et al., 1996). The Bishop Tuff, located in eastern California (Figure 1a), erupted at about 767 ka (766.6 ± 0.4 ka $^{40}Ar/^{39}Ar$ date, Mark et al., 2017, and generally consistent U/Pb zircon ages, see discussion by Ickert et al., 2015) following the collapse of the Long Valley caldera. A large volume (~200 km^3) of high-silica rhyolite erupted over a period of days to a few years (Sheridan & Wang, 2005; Wilson & Hildreth, 1997).

2. Sampling and Methods

2.1. Owens Gorge Outcrop Field Investigations

Samples of the Bishop Tuff were collected in the Owens River Gorge, northwest of Bishop, CA, where several eruptive packages are well exposed with a local thickness up to 170 m. We sampled three vertical profiles (EE, FF, and GG in Table 1), on the eastern wall of the gorge in similar locations as sections E, F, and G of Wilson and Hildreth (2003) to place our paleomagnetic study in the context of their extensive petrologic work on the eruption, composition, and thermal history of the Bishop Tuff. The three vertical sections we sampled show a range of welding conditions, from sintered to densely welded, as well as degrees of postemplacement alteration within eruptive packages Ig1Eb and Ig2Eb of Wilson and Hildreth (1997; Table 1 and Figure 1b). Eruptive package Ig1Eb was erupted earlier and contains few lithics and no pyroxenes compared with Ig2Eb, which contains pyroxenes and 30–70% rhyolite in the lithic component (see Wilson & Hildreth, 1997, for a complete stratigraphic description). Within these eruptive packages there are four maxima in density and therefore in welding; our sections sample two, zones c and d (Figure 1c).

Each profile consisted of more than 20 sites, with 3–4 cores drilled with a portable gasoline powered drill and/or unoriented hand samples collected at each site. The core samples were oriented in situ with a clinometer and magnetic compass, and when possible a Sun compass. GPS (Global Positioning System) location was recorded at the bottom and top of each vertical profile (Table 1), and a Jacob's staff was used to measure the height above the river of each sampling site (above basement rock for profile EE).

At each profile, susceptibility variations were measured (at ~2-m interval) using a portable SM-20 susceptibility meter with nominal sensitivity of 10^{-6} SI. Three measurements were made at each site on the flattest rock surfaces available. Standard deviations for these three measurements average about 15% of the mean susceptibility though this scatter increases at low susceptibility ($<10^{-4}$ SI). The average field susceptibility readings were calibrated using susceptibilities from core samples measured on a Kappabridge KLY-4S and provide a more continuous record of susceptibility variations for the sampled sections.

2.2. Sample Preparation and Preliminary Laboratory Measurements

One or more standard 2.5-cm specimens were cut from each oriented core, and the hand samples were cut into 2.5-cm cubes. The volume and mass of all the specimens were measured in order to calculate their dry-weight densities, as a means to estimate the degree of welding, and in turn, the emplacement temperature and initial thickness (Riehle et al., 1995; Sheridan & Wang, 2005; Wilson & Hildreth, 2003). The anisotropy of magnetic susceptibility (AMS) tensor was measured with a Kappabridge KLY-4S using the AMSSpin software of Gee et al. (2008). AMS is used to test for anisotropy related to emplacement fabric or deformation. The natural remanent magnetization (NRM) of all the specimens was measured with the 2G three axis cryogenic magnetometer at Scripps Institution of Oceanography, University of California–San Diego. Representative pilot specimens from each site were thermally demagnetized to inform selection of temperature steps for the paleointensity experiments. Characteristic remanent magnetization directions were determined by principal component analysis (Kirschvink, 1980) and along with the AMS results are reported and discussed in the supplementary materials section 2.

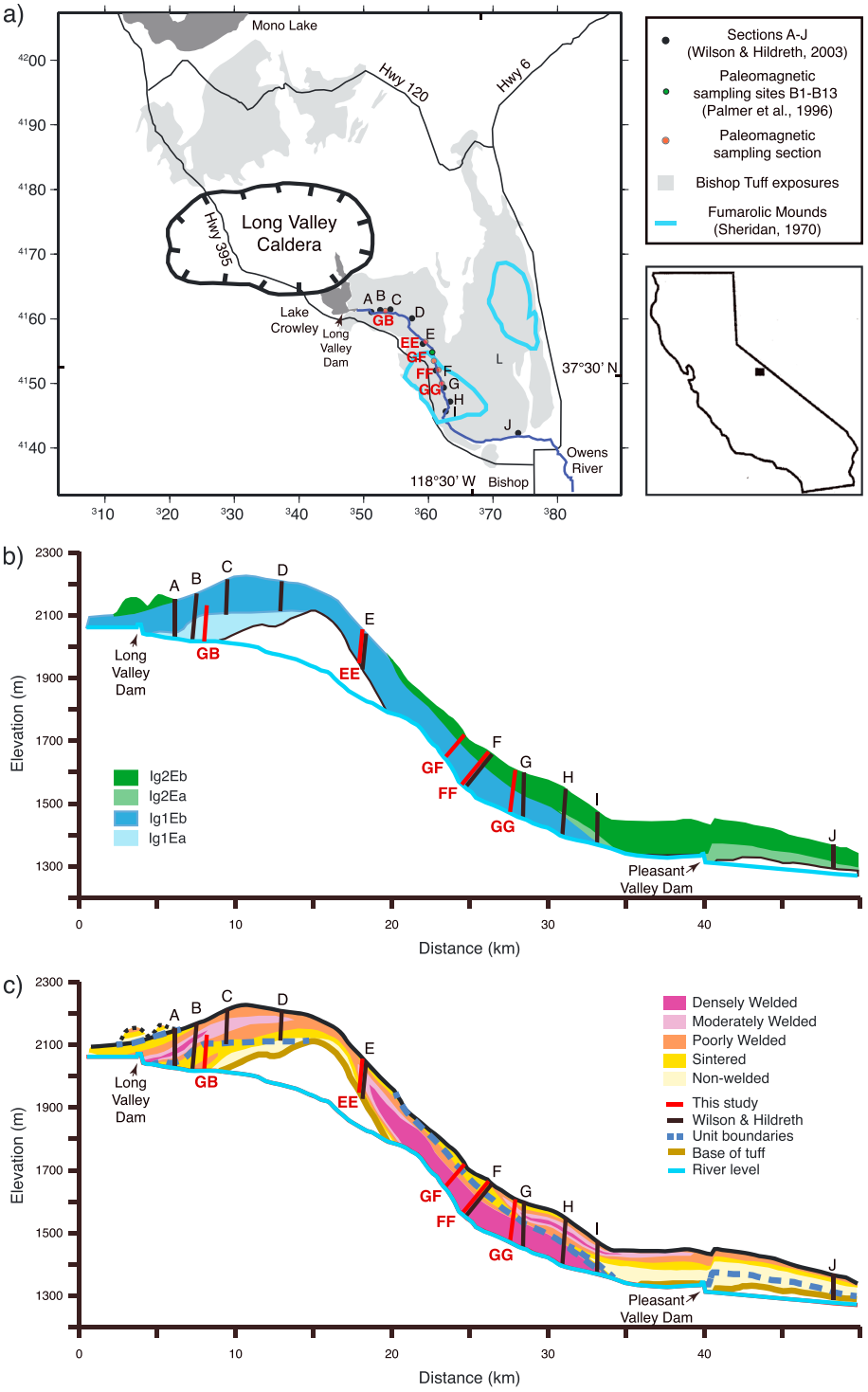

Figure 1. (a) Map of paleomagnetic sampling sections in the Bishop Tuff. Sections EE, FF, and GG were collected as part of this study. GB and GF were sampled previously (Gee et al., 2010). Shown for reference are the location of sections from Wilson and Hildreth (2003), Bishop Tuff outcrop pattern after Wilson and Hildreth (1997), paleomagnetic sampling sites B1-B13 of Palmer et al. (1996), and approximate outcrop of fumarole zones (*Sheridan,* 1970) . b) Profile of flow units of the Bishop Tuff along the Owens River gorge. c) Profile of degree of welding of the Bishop Tuff along the Owens River gorge. Modified from Wilson and Hildreth (2003).

Table 1
Bishop Tuff Sampling Section Descriptions

Section	EE	FF	GG
Eruptive Unit	Ig1Eb	Ig1Eb and Ig2Eb	Ig1Eb and Ig2Eb
Welding (with increasing height)	Non-welded to moderately welded	Ig1Eb – densely welded to sintered Ig2Eb – sintered to poorly welded	Ig1Eb – densely welded to poorly welded Ig2Eb – sintered to densely welded, back to sintered
Alteration zone	Vapor phase zone	Fumarolic mound zone	Fumarolic mound zone
Number of sampling sites	22	25	23
Base Northing	4156654	4151853	4149603 (east) 4149674 (west)
Base Easting	359700	361493	362454 (east) 362016 (west)
Top Northing	4156670	4151833	4149669 (east) 4149718 (west)
Top Easting	359874	361616	362540 (east) 361966 (west)

Note. Welding information is from Wilson and Hildreth (2003), and fumarole information is from Sheridan (1970). Coordinates (WGS84) are given for the base and top of each sampled section. The three sections were designed to parallel sections E, F, and G from Wilson and Hildreth (2003). The top 45 m of section GG was accessed from the western wall of the gorge.

2.3. Paleointensity Experiment

Paleointensity estimates were made at Scripps Institution of Oceanography using the 2G three axis cryogenic magnetometer. We used the IZZI variant of the Thellier-Thellier method (e.g., Tauxe & Staudigel, 2004; Yu et al., 2004) to determine the paleointensity of 55 standard 2.5 cm diameter cores and 381 small chips mounted in glass tubes. Specimens were heated to a maximum temperature of 600 °C or 680 °C when a significant fraction of the remanence remained after 600 °C. A laboratory field of 40 μT was used for the in-field steps. The paleointensity was estimated using the PmagPy Thellier GUI of Shaar and Tauxe (2013) using the autointerpreter tool. For comparison we also reinterpreted the data from the GB and GF sections of Gee et al. (2010) using the Thellier GUI. To reject specimens with poor quality data we used the following selection criteria: the maximum deviation of the partial thermal remanent magnetization (pTRM) check normalized by the length of the best fit line (DRAT $\leq$ 5.0; Selkin & Tauxe, 2000), an estimate of the scatter about the fit line normalized by the slope ($\beta = \sigma/|b| \leq 0.05$, Coe et al., 1978), and the fraction of the total remanence used to calculate paleointensity ($f_{vds} \geq 0.85$, Tauxe & Staudigel, 2004). For reference, the PICRIT03 (Modified) and SELCRIT2 (Modified) sets of selection criteria apply $\beta \leq 0.1$, DRAT ≤ 10, and $f \geq 0.35$ along with other criteria (Paterson et al., 2014). An evaluation of these limits can be found in the discussion section. We used the STDEV-OPT algorithm within the Thellier GUI. This algorithm selects estimates of the ancient field (B_{anc}) that minimize the site standard deviation using all estimates of B_{anc} that pass the criteria.

2.4. Magnetic Mineralogy Experiments

The magnetic mineralogy and rock magnetic properties of the tuff can provide valuable information about whether the NRM is likely thermal or chemical in origin (e.g., the presence of secondary phases such as hematite might suggest a chemical remanence). To determine the magnetic mineralogy, a suite of rock-magnetic properties were measured at the Institute for Rock Magnetism, University of Minnesota. Hysteresis loops and backfield curves were measured on a Princeton Measurements vibrating-sample magnetometer (model 3900 "MicroMag"; sensitivity 5×10^{-9} Am^2) at room temperature, and frequency-dependent susceptibility was measured on the MAGNON Variable Frequency Susceptibility Meter (sensitivity 10^{-5}–10^{-7} SI, depending on frequency, field and sample size). These give information about the domain state of the magnetic minerals. The frequency dependence of susceptibility parameter, χ_{fd}, is determined by $\chi_{fd} = \frac{\chi_{lf}(f_1) - \chi_{hf}(f_2)}{\chi_{lf}(f_1)\log\left(\frac{f_2}{f_1}\right)} \times 100\%$,

where χ_{lf} is the low-frequency susceptibility at frequency f_1, χ_{hf} is the high-frequency susceptibility at frequency f_2, and $f_1 < f_2$. Temperature-dependent susceptibility was measured on the Kappabridge KLY-2

(sensitivity 4×10^{-8} SI) under air, and the minima in the derivatives of the $k(T)$ heating curves were used to determine the Curie temperature of the magnetic minerals (Fabian et al., 2013; Petrovsky & Kapicka, 2006). Low-temperature remanence was measured on the Magnetic Property Measurement System (sensitivity 10^{-11}/Am^2) in order to identify magnetic minerals by low-temperature crystallographic transitions.

Representative samples from about half the sites were given a three-component isothermal remanent magnetization (IRM) and thermally demagnetized (Lowrie, 1990) to further characterize the mineralogy of the remanence-carrying fraction. Stepwise IRM acquisition curves (18 steps from 50 mT to 2.5 T) were measured for these specimens, resulting in a saturation IRM in the sample $+z$ direction. Then the $+y$ and $+x$ directions were subsequently magnetized with a pulse magnetizer at 0.4 T and 0.1 T fields, respectively. The specimens were then thermally demagnetized (19 temperature steps between 100 and 680 °C) and the temperature at which each component was demagnetized by 90% and the relative contribution of each IRM component's demagnetization curve were evaluated.

3. Results

3.1. Density

Density was determined as a proxy for degree of welding, which in turn can be related to the emplacement temperature. An informed estimate of emplacement temperature is critical for interpreting the temperature of remanence acquisition. The density of the specimens varies with stratigraphic height (Figures 2a, 2d, and 2g) and correlates well with densities measured by Wilson and Hildreth (2003). The thermal modeling results of Riehle et al. (1995) indicate that for a simple cooling unit, densities ≥2.0 Mg/m^3 are achieved for thick flows (initial thickness ≥ 80 m) emplaced at temperatures of ≥660 °C. A flow with an initial thickness of 40 m would reach ≥2.0 Mg/m^3 if emplaced at ≥720 °C (for further examples see Figure 8 of Riehle et al., 1995). Within our three sections we sampled welding zones c and d identified by Wilson and Hildreth (2003). In section EE the density increases from about 1.2 Mg/m^3 at the contact with the basement rock to almost 2 Mg/m^3 at a height of 50 m (zone c; Wilson & Hildreth, 2003) and then decreases to 1.45 Mg/m^3 at the top of the section. The density of section FF varies between 2.2 and 2.35 Mg/m^3 (zone c; Wilson & Hildreth, 2003) until a height of ~50 m where it begins to decrease. The lowest density of the FF section, 1.16 Mg/m^3, occurs at 125.7 m (10 m above the boundary between units Ig1Eb and Ig2Eb). Above this level the density increases to 1.5 Mg/m^3 at the top of the section (zone d; Wilson & Hildreth, 2003). Section GG's pattern of density variation starts at ~2.2 Mg/m^3 at the base of the section up until 67.5 m (zone c; Wilson & Hildreth, 2003] where the density decreases rapidly through the flow unit boundary to a local minimum of 1.47 Mg/m^3 at ~80 m (just above the flow boundary at 75 m). The density then increases through the Ig2Eb unit reaching a local maximum of 1.93 Mg/m^3 at 98 m (zone d; Wilson & Hildreth, 2003), then decreases back to ~1.4 Mg/m^3 at the top of the section. Variations in density between profiles are likely due to differences in initial thickness where thicker units welded to higher density [Riehle et al.,1995; Sheridan & Wang, 2005]. For example, welding zone c at section EE, where the thickness of flow Ig1Eb was limited by the basement rock, did not become as densely welded as zone c in sections FF and GG, indicating zone c at section EE cooled more rapidly and spent less time above the threshold temperature for welding. Wilson and Hildreth (2003) discuss the difficulty and nonuniqueness of determining emplacement temperature of ignimbrites, which may be erupted in pulses, but the modeling results of Riehle et al. (1995) and Sheridan and Wang (2005) indicate that 600–660 °C is a reasonable emplacement temperature estimate for units Ig1Eb and Ig2Eb. In the lower portions of sections FF and GG zone c is densely welded, which significantly reduced the porosity and limited exposure of this portion of the ignimbrite to meteoric-hydrothermal alteration (Holt & Taylor, 1998).

3.2. Rock Magnetism and Magnetic Mineralogy

Ignimbrites have potentially complex magnetic remanence due to their cooling and alteration histories, so it is important to characterize the remanence carriers and to evaluate thermal and chemical remanence contributions to the NRM. The first indication of complex rock magnetic properties came from the magnetic susceptibility measurements made in the field (green triangles in Figures 2b, 2j, and 2r). In some sections susceptibility variations broadly parallel density changes, as might be expected if enhanced susceptibility was simply due to increased concentration of magnetic grains during compaction. However, the order of magnitude change in susceptibility in the FF section cannot be explained by compaction alone. The susceptibility increases slightly from the base of the FF section up to a peak at 70 m above the canyon base, then

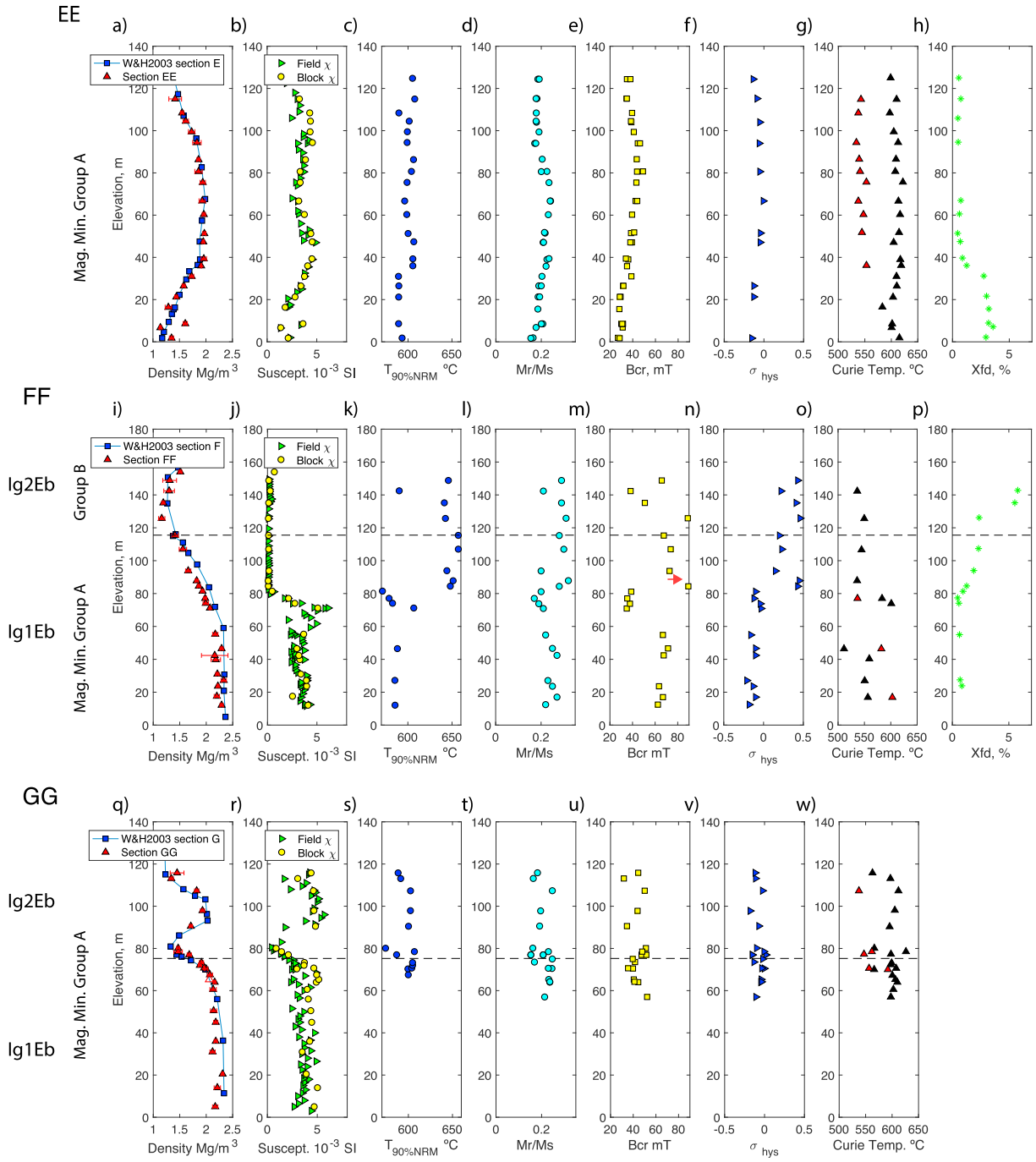

Figure 2. Density and magnetic properties as functions of stratigraphic height. The dashed horizontal lines in sections FF and GG plots are the flow unit boundaries. Flow units Ig1Eb and Ig2Eb, and welding zones c and d are from Wilson and Hildreth (2003). (a, i, and q) The density throughout the EE, FF, and GG sections, respectively. The red triangles are from this study; see text for measurement details. The filled red triangles are site means with the standard deviation. The open red triangle is a site with only one sample available. The blue squares are the density measurements from *Wilson and Hildreth* (2003) for reference. (b, j, and r) The magnetic susceptibility for sections EE, FF, and GG. The green triangles were measured in the field, and the yellow circles were measured on the Kappabridge—see text for measurement details. (c, k, and s) The dark blue circles are the temperature at which 90% of the NRM is removed. (d, l, and t) The cyan circles are M_r/M_s. (e, m, and u) The yellow squares are B_{cr}. The red arrow in (m) indicates a sample with an outlier B_{cr} value of 190 mT. (f, n, and v) The blue triangles are σ_{hys} values according to method of Fabian (2003). M_r, M_s, B_{cr}, and σ_{hys} are defined in the text below. (g, o, and x) The Curie temperatures as determined by the minimum of dk/dT heating curves. The black triangles are the minimum and red triangles are local minima. (h and p) The green stars are frequency-dependent susceptibility over a frequency range of 109–9901 Hz.

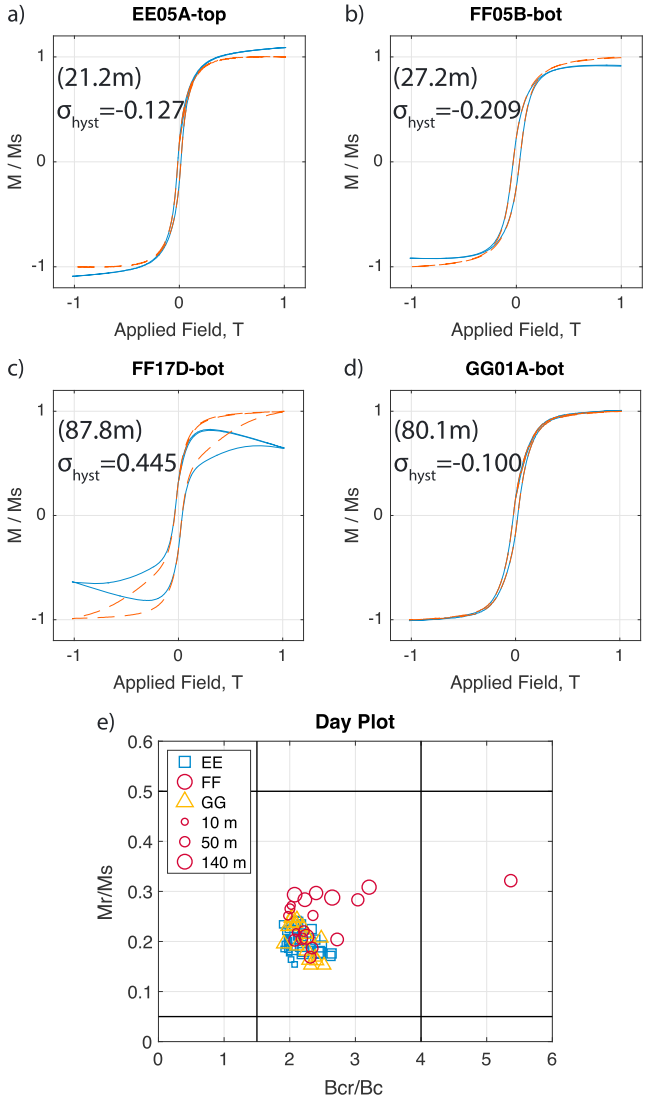

Figure 3. Representative hysteresis loops illustrating (b) pot-bellied, (a and d) normal, and (c) wasp-waisted behaviors. Section EE-site EE05 (a), section FF-site FF05 (b), and site FF17 (c), and section GG-site GG01 (d). The solid blue line is the original curve, and the dashed red line is the high-field slope corrected curve. Additional magnetic results from samples from these same sites are plotted in Figures 4, 5, and 7. (e) Day plot summarizing hysteresis results from all specimens with marker area scaled by stratigraphic height above the base of the unit. The upper portion of FF is distinctly different from the rest of the specimens.

between 70 and 80 m susceptibility decreases rapidly by an order of magnitude, and this low susceptibility continues to the top of the section. A similar drop in susceptibility was observed in section GF in Gee et al. (2010) at 100 m and the pronounced reduction in susceptibility at the top of profiles GF and FF is likely related to vapor-phase alteration. Section EE's susceptibility variation with height has two local highs. The susceptibility in the GG section is generally more scattered than in the other two sections, with a distinct minimum at ~80-m concurrent with the density minimum of that section. The presence of frequency dependence in the magnetic susceptibility can indicate SP populations (i.e., Eick & Schlinger, 1990; Mullins & Tite, 1973; Worm & Jackson, 1999). We observe frequency dependence in magnetic susceptibility in portions of poorly welded tuff (i.e., lower part of section EE and upper part of section FF) that could be due to SP grains (Figures 2h and 2p).

Hysteresis data show a range of behaviors, from slightly pot-bellied to significantly wasp-waisted (Figure 3). In addition to the standard hysteresis parameters (M_r = saturation remanence, M_s = saturation magnetization, B_c = coercivity, and B_{cr} = coercivity of remanence), we calculated the hysteresis loop shape parameter $\sigma_{hys} = \log\left(\frac{E_{hys}}{4M_sB_c}\right)$ following Fabian (2003), where E_{hys} is the area of the hysteresis loop. All of these hysteresis properties vary significantly with stratigraphic height (Figure 2). As with the magnetic susceptibility, the most pronounced change in hysteresis behavior is seen above 84 m in section FF where the hysteresis loops display wasp-waisted behavior ($\sigma_{hys} > 0$) indicative of a mixture of high- and low-coercivity groups, which we interpret as a signal of alteration products with high-coercivity (Roberts et al., 1995; Tauxe et al., 1996). There is a close correspondence between the drop in magnetic susceptibility and an increase in σ_{hys} (Figures 2f, 2n, and 2v). In sections EE, GG, and the bottom of section FF, σ_{hys} is close to zero or slightly negative (pot-bellied). Above 84 m in section FF, σ_{hys} is larger and positive (wasp-waisted). M_r/M_s also increases above 84 m in section FF, and B_{cr} is scattered above 70 m with both high and low values—and one very high value (red arrow in Figure 2m). The bottom of section FF also has high coercivity, with $B_{cr} > 60$ mT, and since B_c is also high the loops from this section are not wasp-waisted. Specimen FF17D-top, from the upper section of FF, was unusually wasp-waisted, so a series of high-temperature hysteresis loops were measured (Figure S2). The low-coercivity phase has a T_c of ~525 °C as most clearly seen in the variation of B_c and σ_{hys} with temperature (Figures S2b and S2c). We interpret the low-coercivity phase as low-Ti titanomagnetite, and the high-coercivity phase as (titano) hematite, so the wasp-waisted behavior is a good indicator of a mixture of (titano) magnetite and (titano)hematite. The Day plot shows a smaller range of values than was measured by Gee et al. (2010). They found M_r/M_s ranging from 0.1 to nearly 0.5 and a tail off to higher B_{cr}/B_c occurring above $M_r/M_s > 0.4$ in samples from their North Canyon sampling section.

The Curie temperatures (T_c) and thermal demagnetization of samples both provide important evidence for identifying the magnetic mineralogy. Temperature-dependent susceptibility [$k(T)$] curves from all samples show the most significant drop in susceptibility at a temperature near the Curie temperature of magnetite. Most specimens display some irreversible $k(T)$ behavior, indicating alteration (Figure 4). We find two principal Curie temperature groups of 520–580 °C and 600–620 °C, with some stratigraphic variability (Figures 2g, 2o, 2w). The black triangles in these panels are the temperatures of minimum dk/dT (Figure 4 insets), and the red triangles denote secondary local minima. In most of section EE (Figure 2g) there are two Curie temperatures present at ~550 and ~610 °C, and the primary T_c on heating is always the higher temperature ~610 °C. This is

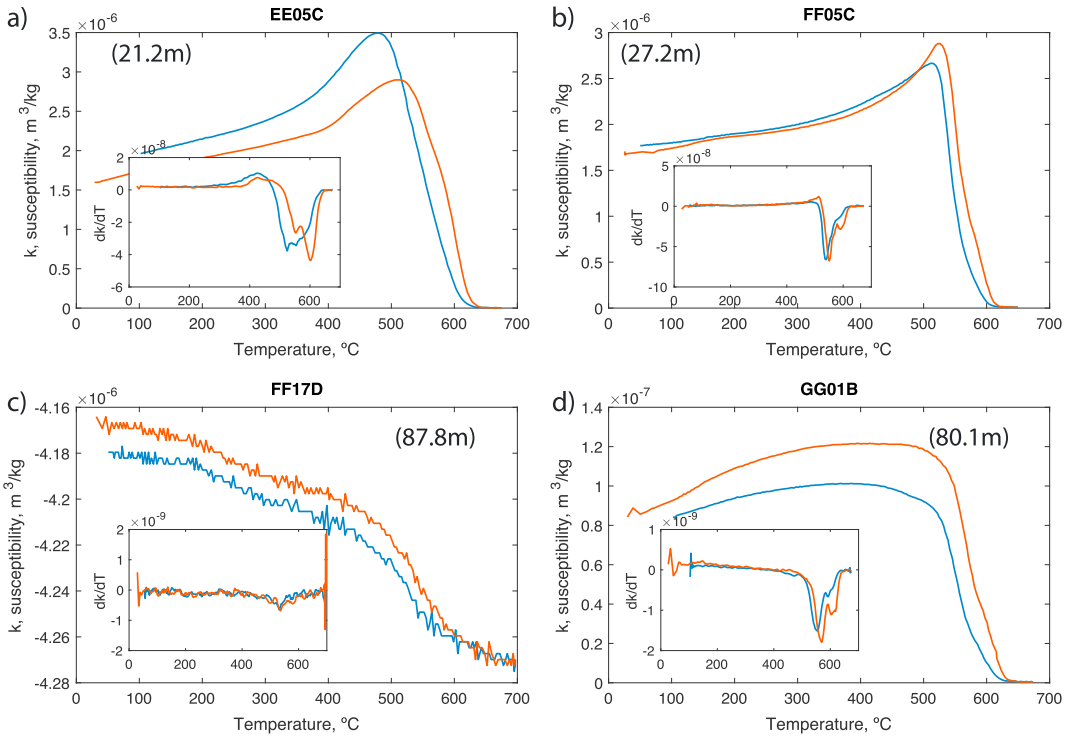

Figure 4. Representative thermomagnetic curves, $k(T)$, and their derivative (insets), dk/dT. Red is the k(T) upon heating, and blue is cooling. (a) Section EE-site EE05, (b) section FF-site FF05 and (c) site FF17, and (d) section GG-site GG01. Results from samples from these same sites are plotted in Figures 3, 5, and 7. The insets show the derivative (dk/dT) curves, smoothed with a moving-window low-order polynomial fitting.

consistent with thermal demagnetization results, with maximum unblocking temperatures slightly above 600 °C (Figure 6a) and 90% of the NRM is demagnetized at a temperature of ~600 °C (Figure 2c). Below 84 m in section FF there are also two Curie temperatures, though these data are more scattered and in two of three cases the secondary T_c (red triangle) is higher than the primary T_c (black triangle). Above 84 m in section FF there is a single T_c at ~550 °C (Figure 2o). The susceptibility is weaker in this section of tuff and therefore the $k(T)$ and dk/dT curves are noisier (Figure 4c) so other Curie temperatures, such as that of hematite, may be masked. Thermal demagnetization of samples from the upper portion of section FF reveals significant remanence with unblocking temperatures from 600 to 675 °C (Figure 5c). The presence of a high unblocking temperature phase is corroborated by the fact that 90% of the NRM is not demagnetized until a temperature of ~640 °C (Figure 2k). In section GG there are a few Curie temperatures near 550 °C, but most are >590 °C (Figure 2w). Like sections EE and the bottom of FF, thermal demagnetization results from section GG show 90% of the NRM is demagnetized at a temperature of ~600 °C (Figure 2s). Despite the variable magnetic mineralogy, specimens from all three sections generally display a single-component remanence, with only a minor overprint that is removed by the 250 or 300 °C heating step (Figure 5).

Thermal demagnetization of a three-component IRM (Lowrie, 1990) also corroborates these two principal temperature groups of 520–580 °C and 600–620 °C (Figure 6). We find the top of section FF has a larger contribution of a magnetic mineral with high-coercivity and with a 90% unblocking temperature of ~640 °C. Most specimens reach saturation isothermal remanent magnetization (sIRM) by 400 mT, except for specimens from section FF above 84 m that may not be saturated even in a 1.0 T field (Figure 6d). The relative contribution of each IRM component's demagnetization curve is represented by the parameter F_n: the fraction of demagnetization curve area. The area, A_n, under the demagnetization curve of each component, n, is normalized by the sum of the areas ($A_x + A_y + A_z$), so $F_n = A_n/(A_x + A_y + A_z)$, where $n = x$, y, and z. The hard fraction (z direction) with coercivities >400 mT (max applied field was 2.5 T) generally carries little of the magnetization, except above 84 m in the FF section where F_z = 20–50% of the remanence (Figure 6f). The hard fraction is 90% demagnetized at a temperature of ~650 °C (Figure 6e). This exemplifies the value of

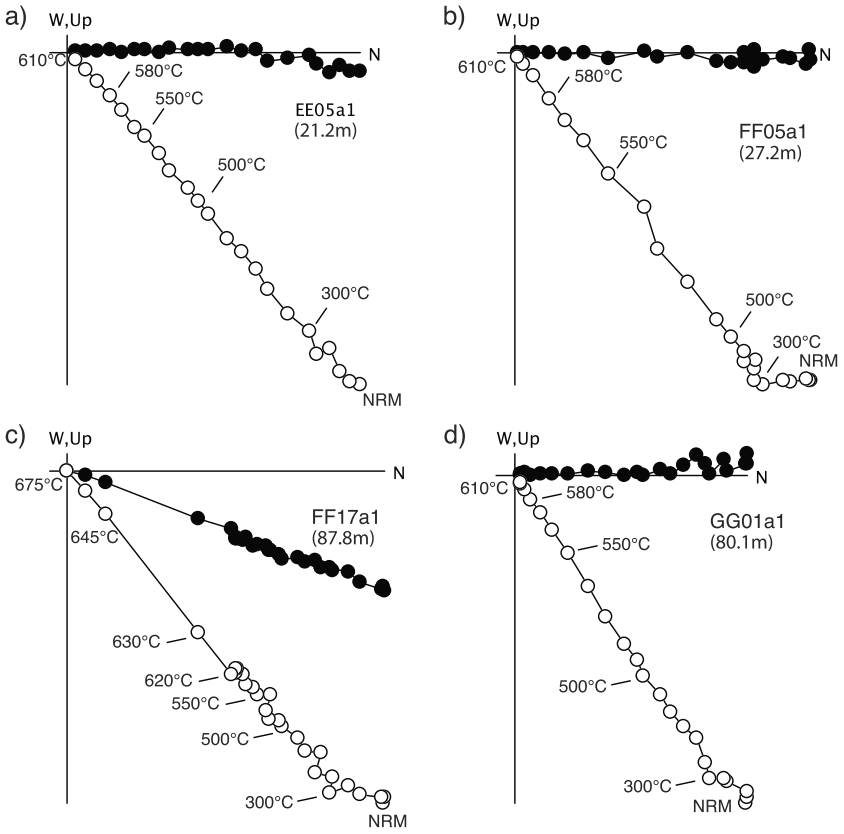

Figure 5. Vector endpoint diagrams illustrating thermal demagnetization results for four representative samples. The filled (open) circles are horizontal (vertical) projections. (a) Section EE-site EE05, (b) section FF-site FF05 and (c) site FF17, and (d) section GG-site GG01. Results from samples from these same sites are plotted in Figures 3, 4, and 7.

the three-component IRM experiment in revealing unblocking that was masked by noise in some $k(T)$ curves above (Figure 4c). The intermediate-fraction (y direction), which contains minerals with coercivities between 100 and 400 mT, carries a significant fraction of the remanence, F_y = 10–40%. This component is 90% demagnetized at temperatures between 520 and 550 °C, although above 84 m in FF several sites have remanence in the y direction remaining above 600 °C. The soft fraction, with coercivities $<$100 mT, carries the majority of the magnetization except above a height of 84 m in FF, where F_x ~ 50%. It is 90% demagnetized consistently at temperatures between 515 and 565 °C.

The Magnetic Property Measurement System low-temperature experiments generally show evidence of maghemitized low-Ti titanomagnetite. The Verwey transition was determined with the warming curve of a low-temperature (10 or 20 K) SIRM for four samples from each section (Figure S3). A smeared and suppressed Verwey transition is a hallmark of maghemitization (Özdemir & Dunlop, 2010) and is observed throughout the tuff except in sample FF17D, which shows no Verwey transition. The Morin transition is evaluated by zero-field thermal cycling of room temperature sIRM. There is no evidence of a Morin transition (263 K) indicating a lack of pure hematite; a small amount of Ti substitution (1 mol%) will suppress the Morin transition temperature to $<$10 K (e.g., Ericsson et al., 1986), as will nanometric grain sizes (Özdemir et al., 2008).

3.3. Paleointensity

Our Thellier-Thellier experiment produced a range of results: 34% of the specimens have nearly straight Arai plots (Figures 7b–7d), 46% are concave upward (Figure 7a), 4% are scattered, 4% are hinged with two distinct slopes at low temperature and high temperature (Figure 7e), and 11% are curved (Figure 7f). We chose reliability criteria to pick specimens that do not alter during the experiment (DRAT $\leq$ 5.0), do not have scattered Arai plots ($\beta \leq 0.05$), and paleointensity estimates that are based on a large fraction of the remanence

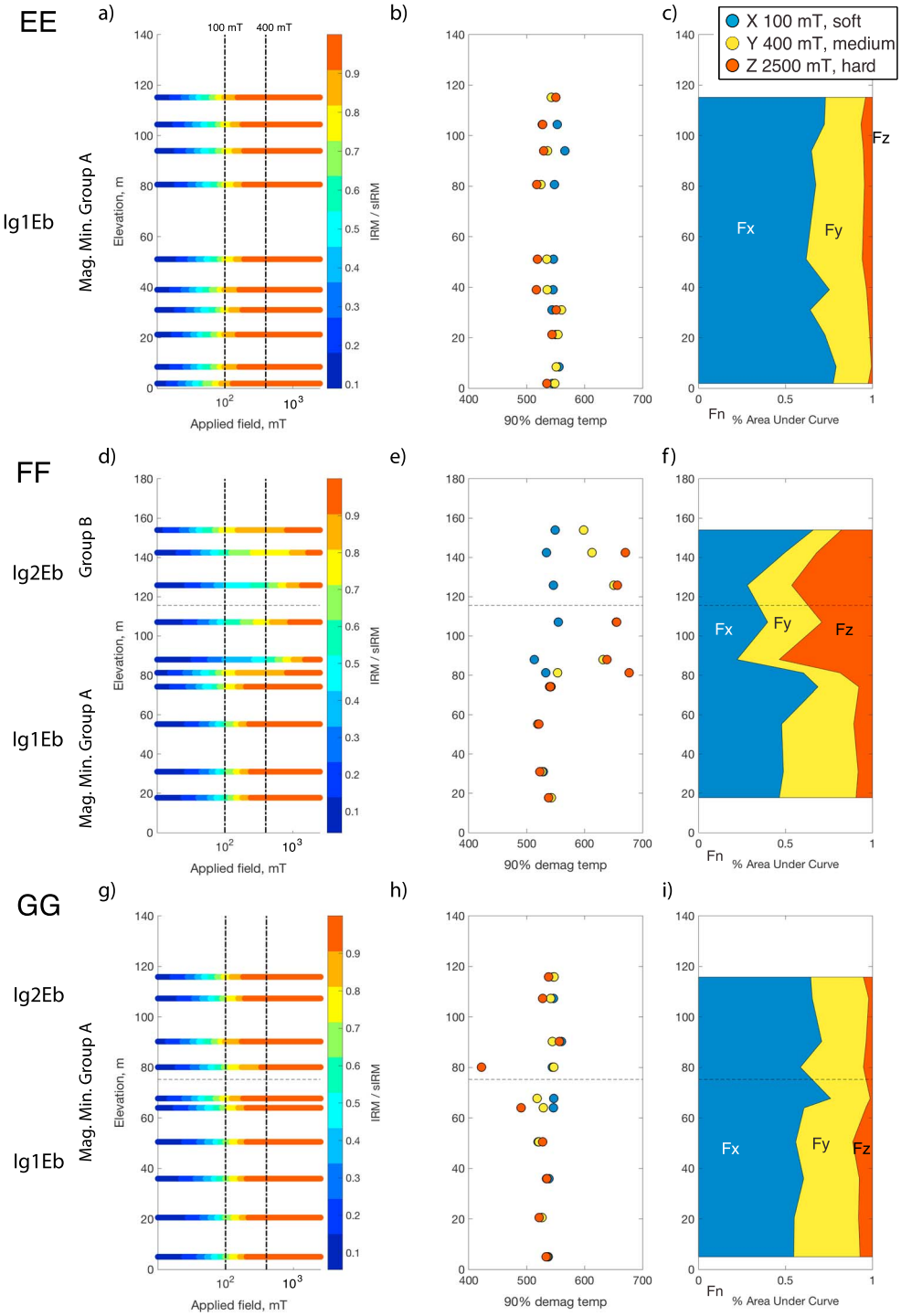

Figure 6. Summary of IRM acquisition and unblocking of a three-component IRM from stratigraphic profiles in Bishop Tuff. (a, d, and g) IRM acquisition curves as a function of height. The color indicates the IRM/sIRM with red = 90–100%, and the dot dashed lines are at 100 and 400 mT, the fields used to impart IRMs along the *x* and *y* directions. (b, e, and h) The 90% unblocking temperatures for the three components of the IRM as a function of height. (c, f, and i) The percentage of the area under the demagnetization curve of each component as a function of height.

($f_{vds} \geq 0.85$). Of the 436 specimens measured, 142 specimens from 33 sites produced one or more temperature ranges that passed these strict selection criteria. Of the 62 specimens from sections GB and GF that were reinterpreted with these selection criteria, 28 specimens from nine sites within section GF

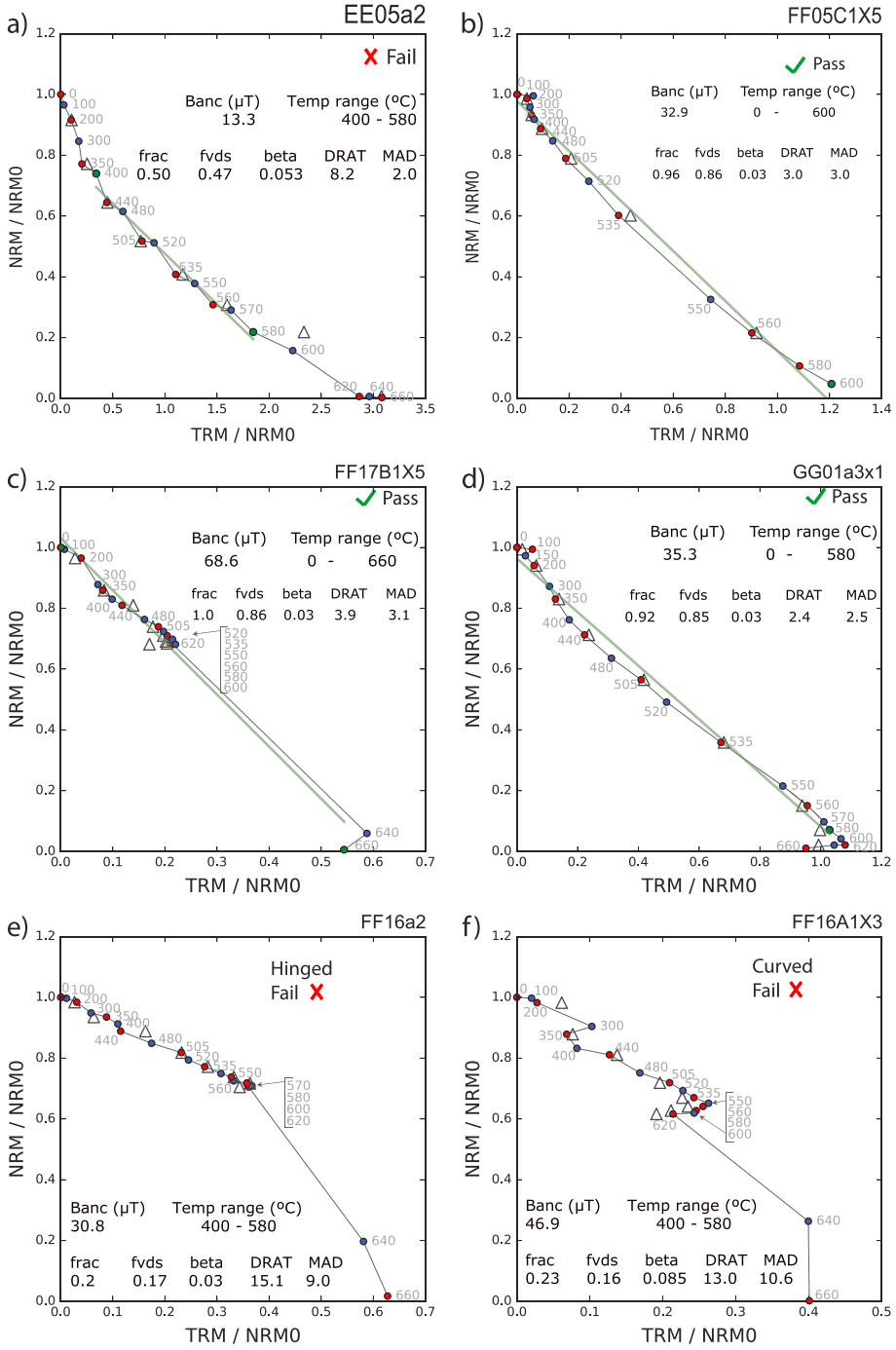

Figure 7. Representative Arai plots. Zero-field followed by in-field cooling (ZI) steps are shown in blue, and in-field followed by zero-field (IZ) steps are shown in red. The pTRM checks are shown with triangles. The green fit-lines indicate the slope used to compute B_{anc} and were chosen by the Thellier GUI to minimize the site level standard deviation. (a–d) These samples were chosen because they are representative of the behavior of that section of tuff; results from samples from these same sites are plotted in Figures 3, 4, and 5. (e and f) These samples represent some typical nonideal behaviors that fail our experiment.

passed. There were no passing estimates from sections GB or EE. The Arai plots from the GB and EE sections, and some specimens from the other sections, are concave (Figure 7a), and had a failing β if their f_{vds} was acceptable—or vice versa. The trade-off between $\beta \leq 0.05$ and $f_{vds} \geq 0.85$ also excludes some specimens from the top of section FF with hinged Arai plots, where the slope above the 580 °C heating steps is much

Table 2
Average Paleointensity Estimates for Various Groupings of the 42 Passing Site Estimates Based of Sampling Location or Density

Group	Number of sites	Mean of site means (μT)	Standard deviation of site means (μT)	Standard error of site means (μT)	Minimum passing estimate (μT)	Maximum passing estimate (μT)
All	**42**	**41.9**	**11.8**	**1.8**	**16.3**	**81.5**
GF	9	44.6	2.4	0.8	40.0	49.9
FF	18	46.6	14.2	0.6	25.9	81.5
GG	15	34.7	8.2	2.1	16.3	52.4
FF < 75 m	9	33.7	3.9	1.3	25.9	49.5
FF > 75 m	9	59.5	6.4	2.1	40.1	81.5
Density > 2.0 Mg/m^3	21	39.6	9.9	2.2	16.9	75.0

Note. The mean of site means is a simple mean; we did not weight by the scatter about the sites.

steeper (Figure 7e). Specimen and site level data can be found in Tables S1 and S2, where we report additional criteria (g_{max}, MAD, DANG, q, and k') and site mean, standard deviation, and standard error. Site means according to section and density can be found in Table 2. Many specimens had multiple temperature ranges that passed the selection criteria. We used the STDEV-OPT algorithm within the Thellier GUI to select the temperature range, which minimized the site standard deviation. These different passing paleointensity estimates from the same specimen should be similar, and indeed, the mean of this within-specimen variation is 1.6 μT. The site standard deviation ranges from 0.05 to 10.1 μT, with errors reported at one standard deviation. Sites from section GF have much smaller scatter than sections FF and GG (Figure 2). We attribute this difference in scatter to our sample collection methods. In the Gee et al. (2010) study, when section GF was collected, an oriented block sample was collected at each site and cores were drilled from the blocks. In this study our collection sites, where oriented cores were collected, had a larger spatial coverage. Cores were collected within about a meter, but over a larger area than a block sample. Our study should better represent the scatter in B_{anc} due to meter-scale heterogeneity

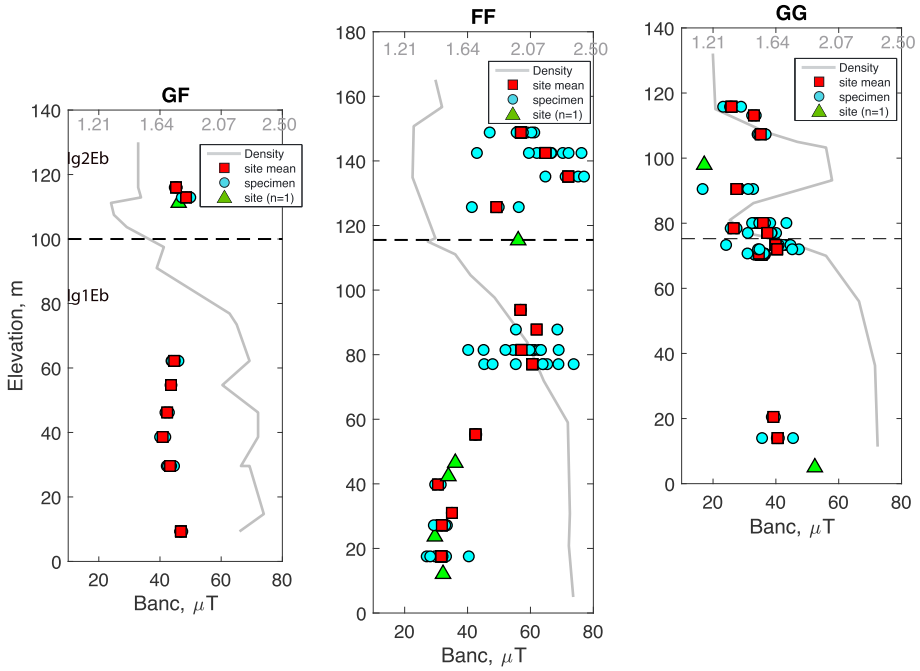

Figure 8. Ancient field (B_{anc}) estimates found using our strictest criteria: $\beta \leq 0.05$, DRAT ≤ 5, and $f_{vds} \geq 0.85$ as a function of height. The red squares are site means, the blue circles are specimen estimates, and the green triangles are specimen estimates for sites with only one passing specimen. The grey line is bulk rock density for reference, with upper scale bar indicating the density values. The dashed line indicates the boundary between eruptive units lg1Eb and lg2Eb of Wilson and Hildreth (1997).

within the Bishop Tuff. The site with the largest scatter is FF14 (78 m) in the FF section. Above this height in the FF section the estimates of B_{anc} are generally higher and more scattered than those from below 78 m (Figure 8). The mean of all 42 sites means is 41.9 ± 11.8 μT. This agrees with the 43.0 ± 3.2 μT value of Gee et al. (2010), but with significantly larger scatter. We add an additional filter of ignimbrite density to select estimates from high density (density ≥ 2.0 Mg/m^3, and therefore low porosity) portions of the ignimbrite under the assumption that these samples have experienced minimal vapor-phase alteration. This produces an estimate for paleointensity of 39.6 ± 9.9 μT.

4. Discussion

As the body of work assessing ignimbrites as a recording material for paleointensity grows, there is mounting evidence that their postemplacement histories have a significant effect on their ability to preserve accurate records of paleointensity. The timing and nature of remanence acquisition in ignimbrites need to be assessed for confident interpretation of their paleointensity data. Disturbingly, we see evidence that a non-TRM remanence may produce a technically reliable paleointensity estimate even with increasingly strict selection criteria. In the Bishop Tuff we find a stratigraphic variation in magnetic mineralogy and paleointensity estimates, both of which are linked to the tuff's thermal history and alteration.

4.1. Thermal History and Magnetic Mineralogy

The rock magnetic results presented above provide evidence for a complex magnetic mineralogy—including low-Ti titanomagnetite, maghemite, and (titano) hematite—that is broadly consistent with earlier results from the Bishop Tuff (Palmer et al., 1996). These authors found that Ti-poor titanomagnetite and maghemite were the dominant carriers in most portions of the ignimbrite, with microcrystals of these Fe-Ti oxides present along shard and pumice boundaries as well as in cleavage planes of biotite and hornblende phenocrysts. Curie temperatures above 600 °C have been attributed to the presence of thermally-stable maghemite in the Bishop Tuff (Gee et al., 2010; Palmer et al., 1996) as well as in other ash flow tuffs (Reynolds, 1977; Rosenbaum, 1993). Palmer et al. (1996) also found evidence for hematite and hematite-rutile in samples from their B1-B13 section, located about midway between our FF and EE sections, 2.5 km north of section FF. The upper part of their B1-B13 section was completely devitrified by vapor-phase crystallization, and they interpreted the low susceptibility as evidence of the destruction of microcrystals and more highly oxidized phenocrysts.

Following Gee et al. (2010) we divide our samples into groups based on magnetic mineralogy, which are broadly correlated with stratigraphy. Group A is found at the top (above ~80 m) of section FF as well as at the top of the previously sampled GF section within eruptive unit Ig2Eb. These samples are characterized by the presence of a significant high-coercivity and high unblocking temperature phase (interpreted as an impure hematite or titanohematite) together with a lower coercivity phase that we interpret as a low-Ti titanomagnetite. Wasp-waisted hysteresis loops ($\sigma_{hys} > 0$) are common in group A samples (Figure 2n), reflecting the presence of a mixture of high- and low-coercivity phases. The high temperatures (~650 °C) at which 90% of the NRM (Figure 2l) and 90% of the high-coercivity component of the three-component IRM (Figure 6e) are unblocked are consistent with a substantial volumetric contribution from hematite. Although maximum unblocking temperatures reach 675 °C (Figure 5c) suggestive of pure hematite, the lack of an obvious Morin transition in many samples indicates that this high-coercivity phase is an impure hematite (possibly a titanohematite) or nanophase hematite (Özdemir et al., 2008). Because of the low susceptibility, the *k*(T) curves from group A samples are noisy and no Curie temperature compatible with hematite was noted. Instead, group A samples have a single Curie temperature of ~540 °C, consistent with the presence of a low-Ti titanomagnetite. The temperature-dependent hysteresis data from a group A sample (Figure S2) are also consistent with a lower coercivity phase with a Curie temperature of about 525 °C. Finally, the 90% unblocking temperatures of the lower-coercivity components of the three-component IRM (Figure 6e) also are compatible with a low-Ti titanomagnetite.

Group B Magnetic Mineralogy is found in sections EE and GG and the lower portions of sections GF and FF. Group B is interpreted as having a remanence carried by fine-grained, low-Ti (titano) magnetite and (titano) maghemite. Results from the Lowrie three-component IRM demagnetization reveal that group B has much less, if any, contribution from high-coercivity phases (Figure 6). The absence of high-coercivity phases is also supported by the hysteresis loops, which tend to have slightly negative σ_{hys} values (Figure 2). The pot-bellied loops may indicate the presence of SD particles (e.g., the classic Stoner-Wohlfarth model SD loop, Stoner &

Wohlfarth, 1948, is pot-bellied) or a mixture of two low-coercivity phases (e.g., SD and fine SP grains; Tauxe et al., 1996). Group B has two Curie temperature groups at 520–580 °C and at 600–620 °C. Most group B samples have a smeared Verwey transition, indicating partial maghemitization where only the surface of the titanomagnetite crystal lattice is oxidized (Dunlop & Özdemir, 2015). Together with the persistence of remanence unblocking to slightly above 600 °C (Figures 2and 5), this suggests that the higher Curie temperature phase is likely an oxidized (titano) maghemite that is thermally stable.

The Bishop Tuff contains two types of low-Ti titanomagnetite: phenocrysts and microcrystals, which we interpret to have grown within the glass after emplacement. We interpret the primary remanence carrier of mineralogy group B to be fine-grained, low-Ti titanomagnetite consistent with the microcrystals at shard boundaries and along cleavage traces of ferromagnesian silicates observed by Palmer et al. (1996), which they suggest are similar to the microcrystals characterized by Schlinger, Rosenbaum et al. (1988). What Palmer et al. (1996) called magnetite and maghemite are consistent with our Ti-bearing versions. Schlinger, Rosenbaum et al. (1988) observed microcrystals of cubic Fe-oxide in the Tiva Canyon Member of the Paintbrush Tuff using transmission electron microscopy imaging, and energy-dispersive X-ray spectroscopy analyses indicated the microcrystals had ~10 mol% Ti. In their study of single zircon crystals from the Bishop Tuff sampled at our GF section at a height of 35 m, Fu et al. (2017) used backscatter electron, quantum diamond microscope, and wavelength dispersion spectroscopy Fe-element microscopy methods to map the ferromagnetism of the zircons and found magnetite or maghemite within and around apatite inclusions. These microcrystal observations are consistent with our T_c = 520 °C–580 °C population. Titanomagnetite phenocrysts are common in the Bishop Tuff but are unlikely to contribute significantly to the remanence of samples that yielded successful paleointensity estimates. Titanomagnetite constitutes only 0.05–0.5% of the total phenocryst assemblage (total phenocrysts range from $<$1% to 24%) and therefore less than 0.1% by volume of tuff samples (Hildreth & Wilson, 2007). The titanomagnetite phenocryst composition is relatively uniform, with ulvöspinel contents of 25–28 mol% (TM25-TM28) (Hildreth, 1979). If unoxidized, these grains should have Curie temperatures $<$450 °C (e.g., Dunlop & Özdemir, 2001 pg. 62). Specimens with substantial ($>$30%) unblocking of NRM below 450 °C are found mostly in section EE and are associated with concave Arai plots (Figure 7b), which is consistent with the presence of multidomain-sized crystals. Most samples have $<$20% unblocking below 450 °C, which suggests that titanomagnetite phenocrysts of this composition do not contribute much to the total remanence. It is possible that the titanomagnetite phenocrysts have been maghemitized to produce a T_c = 520 °C–580 °C. There is also evidence of oxyexsolution; though there are some un-oxyexsolved grains present as FeTi oxide pairs have been used for geothermometry, and estimate a pre eruptive magma reservoir temperature of 714–818 °C (Evans et al., 2016; Hildreth, 1979; Hildreth & Wilson, 2007).

For conducting Thellier-Thellier type paleointensity experiments we need to consider the origin of these minerals and the nature of their remanence, whether TRM, pTRM, CRM, or TCRM. Sheridan and Wang (2005) modeled density profiles from north and east of the Long Valley caldera and calculated the emplacement temperature to be typically ~650 °C, and significant welding and density $\geq$ 2.0 Mg/m^3 to indicate the tuff was emplaced at temperatures above 660 °C. After emplacement the ash flow can viscously deform, compact, and flatten while above the glass transition temperature, T_g (Sheridan & Wang, 2005). The welding is controlled by the time-temperature-pressure path followed by the flow, with densely welded sections typically having spent more time at higher temperatures. Thicker sections are more likely to develop dense welding because of the greater pressures and slower cooling rates. So the densely welded material found in sections GF, FF, and GG spent more time at higher temperatures.

The fine-grained titanomagnetites may have precipitated after emplacement (Geissman et al., 1983; Schlinger, Rosenbaum et al., 1988; Schlinger, Griscom et al., 1988), and if this occurred above their T_c, they would record a TRM. The presence of welding or partial welding also strongly suggests the flow was emplaced above T_g, which depending on the water content of the flow occurs at ~550–600 °C (Giordano et al., 2005). Minimum estimates of temperature required for welding vary from 575 °C to over 600 °C (Grunder et al., 2005; Riehle et al., 1995), which are higher than the T_c of the low-Ti titanomagnetite (T_c = 520 °C–580 °C) we find as the main remanence carrier for group B. Titanomagnetite microcrystals could precipitate at temperatures above T_g, and below T_c of titanomagnetite ($T_g < T < T_c$) and such microcrystals would carry a TCRM (Gee et al., 2010).

Below T_g, remanence acquired during cooling would be a pTRM. Models show that compaction of ignimbrites occurs over weeks to 2–3 years, and temperatures near emplacement temperatures can last for decades depending on the flow thickness and amount of rainfall (Riehle, 1973; Riehle et al., 1995). Magnetic remanence would be acquired on a similar time scale, and this could dramatically impact Curie and blocking temperatures of moderate-Ti titanomagnetites via crystal-chemical reordering (Bowles et al., 2013; Bowles & Jackson, 2016; Jackson & Bowles, 2014). Fortunately, the titanomagnetite here is low in Ti and we see no evidence of the unstable remanence due to cation reordering observed in the Mt. St. Helens ignimbrites.

The (titano) hematite in mineralogy group A is likely a product of postemplacement alteration. The products of vapor-phase alteration are altered phenocrysts, precipitates in cavities and coatings of magnetite as well as hematite and goethite (Keith, 1991; Keith & Muffler, 1978). Hematite and goethite are also found to replace both phenocryst and vapor-phase magnetite (Keith & Muffler, 1978). Holt and Taylor's (1998) section CG (roughly coincident with our GF section) showed $\delta^{18}O$ varies considerably with depth within the fumarole zone, where values are dramatically depleted due to meteoric-hydrothermal alteration. Holt and Taylor (1998, 2001) found groundmass with depleted oxygen isotopes coincident with feldspar phenocrysts that preserve their magmatic $^{18}O/^{16}O$ ratio. This shows vapor-phase alteration occurs during initial short-lived high-temperature ($>$500 °C) exchange with meteoric water, followed by longer exchange at lower temperature ($<$150 °C). The welded units in Bishop Tuff restrict this $\delta^{18}O$ depletion, so the more densely welded material lower in the same sections may not have experienced this alteration because of their lower permeability (Holt & Taylor, 1998). Columnar jointing found in the upper nonwelded portions of the deposit is also evidence of devitrification and vapor-phase crystallization (Wright et al., 2011), the columnar jointing is discussed further in the supplementary materials section 2.

The (titano) maghemite found in group B was formed by oxidation of titanomagnetite. The timing of this oxidation is not clear. The presence of maghemitization in the densely welded lower portions of sections FF, GF, and GG indicates that it was not associated with an exchange with hydrothermal fluids, as these portions of the Bishop Tuff experienced little exchange with meteoric hydrothermal fluids (Holt & Taylor, 1998). The oxidation may have occurred below the T_c of titanomaghemite (610–620 °C) in which case the NRM would be in part a TCRM acquired under the combined effects of chemical change and temperature decrease. The titanomaghemite has a consistent T_c of 610–620 °C throughout the tuff, which may indicate the oxidation to titanomaghemite, was preeruptive rather than due to postemplacement alteration, although it is generally thought that single-phase titanomagnetite can sustain only a limited amount of nonstoichimetry at high temperature (e.g., Senderov et al., 1993), and that high degrees of homogeneous oxidation occur at near ambient T (e.g., Özdemir & Dunlop, 2010 and references therein).

Due to the Bishop Tuff's complex thermal history, the NRM of some specimens is likely a mixture of thermal and chemical remanences. Our primary concern in this study is to determine if a CRM or TCRM are able to produce paleointensity estimates of high technical quality that are different from the true paleointensity, which for ancient flows is unknown. Draeger et al. (2006) showed experimentally that CRM and TCRM can produce semilinear Arai plots and that a CRM will underestimate paleointensity if treated as TRM. Their samples with a CRM had concave Arai plots at low temperatures with more NRM lost than pTRM gained. Fabian (2009) shows theoretically a CRM due to isothermal SD grain growth underestimates paleointensity; a TCRM due to dissolution of the remanence carrying minerals after TRM acquisition overestimates paleointensity, and a TCRM due to low-temperature oxidation after TRM acquisition also overestimates paleointensity. Theoretically, TCRM in both cases would have straight Arai plots.

4.2. Paleointensity Interpretation

Here we test a range of selection criteria (with variable β, DRAT, and f_{vds}) to filter out the nonideal Arai plot behaviors. To assess the effect of these criteria we plot the cumulative distribution functions (CDFs) for these reliability criteria (Figures 9a–9d), and plot the B_{anc} estimate versus the reliability criteria value for each passing specimen (Figures 9e–9h). We initially apply loose criteria ($\beta \leq 0.1$, DRAT ≤ 10, and $f_{vds} \geq 0.5$) to filter the most nonideal data (red lines Figures 9a–9d and red triangles Figures 9e–9h). For our 498 specimens analyzed β, DRAT, and f_{vds} filter out the most extreme B_{anc} estimates, but there is a large range of paleointensities and a non-Gaussian paleointensity CDF with two steep sections at ~40 and ~60 μT (Figure 9a).

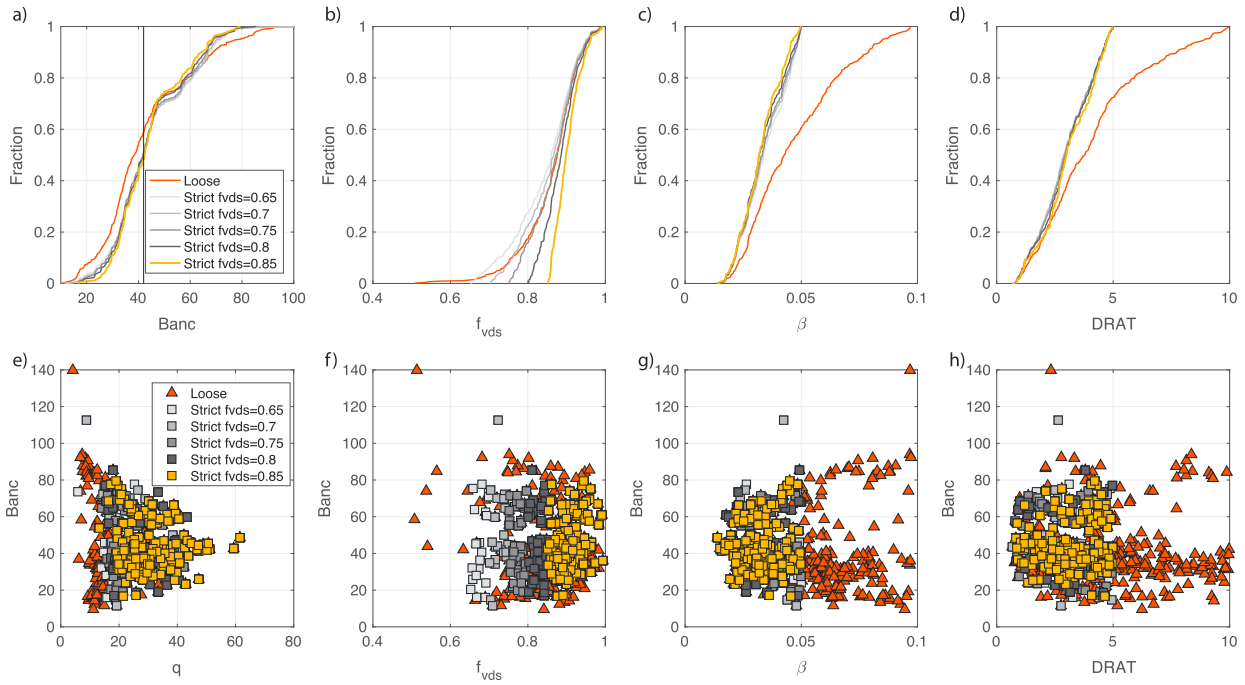

Figure 9. The effect of the selection criteria on the B_{anc} data set. (a–d) Cumulative distribution functions (CDFs) of B_{anc} estimates, f_{vds}, β, and DRAT. (a) The vertical line is 41.9 μT, the mean B_{anc} from Gee et al. (2010), for reference. (e–h) B_{anc} as a function of q (Coe et al., 1978, quality factor), f_{vds}, β, and DRAT. The red lines and triangles are B_{anc} estimates that pass loose selection criteria: $\beta \leq 0.1$, DRAT ≤ 10, and $f_{vds} \geq 0.5$. The gray lines and squares are estimates that pass strict selection criteria: $\beta \leq 0.05$, DRAT ≤ 5, and $f_{vds} \geq 0.65$–0.80. The yellow lines and squares are estimates that pass strictest selection criteria: $\beta \leq 0.05$, DRAT ≤ 5, and $f_{vds} \geq 0.85$.

We next applied stricter criteria ($\beta \leq 0.05$, DRAT ≤ 5, and $f_{vds} \geq 0.65$), and we increased our f_{vds} threshold in increments of 0.05 to reject the hinged behavior, which produces high paleointensities (grey lines Figures 9a–9d and grey squares Figures 9e–9h). Even $f_{vds} \geq 0.85$ does not filter out all the paleointensity estimates >52 μT (yellow lines in Figures 9a–9d and yellow squares in Figures 9e–9h). We also applied the CCRIT selection criteria (Cai et al., 2017; Cromwell et al., 2017; Tauxe et al., 2016) ($\beta \leq 0.1$, DANG ≤ 10°, MAD ≤ 5°, FRAC ≥ 0.78, SCAT = pass, $|k'| \leq 0.164$, gap max ≤ 0.6, $N > 3$, and σ% ≤ 10%) to test the impact of gap max and curvature criteria. Using the CCRIT criteria also produces paleointensity estimates >52 μT (Figure S4). These high B_{anc} estimates are of good technical quality. We interpret the remanence in the top of the FF section as TCRM, but our paleointensity experimental protocol alone does not reveal this. To facilitate discussion, we define paleointensity groups: type 1 with $B_{anc} < 35$ μT, type 2 with B_{anc} = 35–52 μT, type 3 with $B_{anc} > 52$ μT.

Some potential sources of scatter and uncertainty in the paleointensity data include cooling rate differences and magnetic anisotropy. The difference between the laboratory cooling (<1 h) and the natural cooling rate, which is thought to be decades for the Bishop Tuff, could cause a ~20% overestimate of paleointensity (Halgedahl et al., 1980), and is a possible source of scatter in the B_{anc} estimates. Anisotropy of TRM is another potential source of scatter, which we have not corrected for. Samples in the lower densely welded portion may have more internal fabric and be more anisotropic compared to specimens from higher in the stratigraphy. During the Thellier experiment the majority, 66%, of specimens which produced estimates of B_{anc} (i.e., those listed in Table S1) had pTRM directions, which agreed with the vertical applied field direction. The largest deviation from vertical was to 11.3 ± 1.6°, where the reported error is the pTRM MAD. In the specimens with pTRM directions that disagreed with vertical, this could indicate anisotropy that could contribute to both shallower than expected characteristic remanent magnetization inclinations (described in section 2 of the supplementary material) and scatter in paleointensities.

Both the magnetic mineralogy subgroups and paleointensity subgroups are broadly correlated with stratigraphic and cooling units. All specimens from sections GB and EE have concave Arai plots with positive pTRM checks suggesting they contain abundant coarse-grained FeTi oxides. Paleointensity estimates from

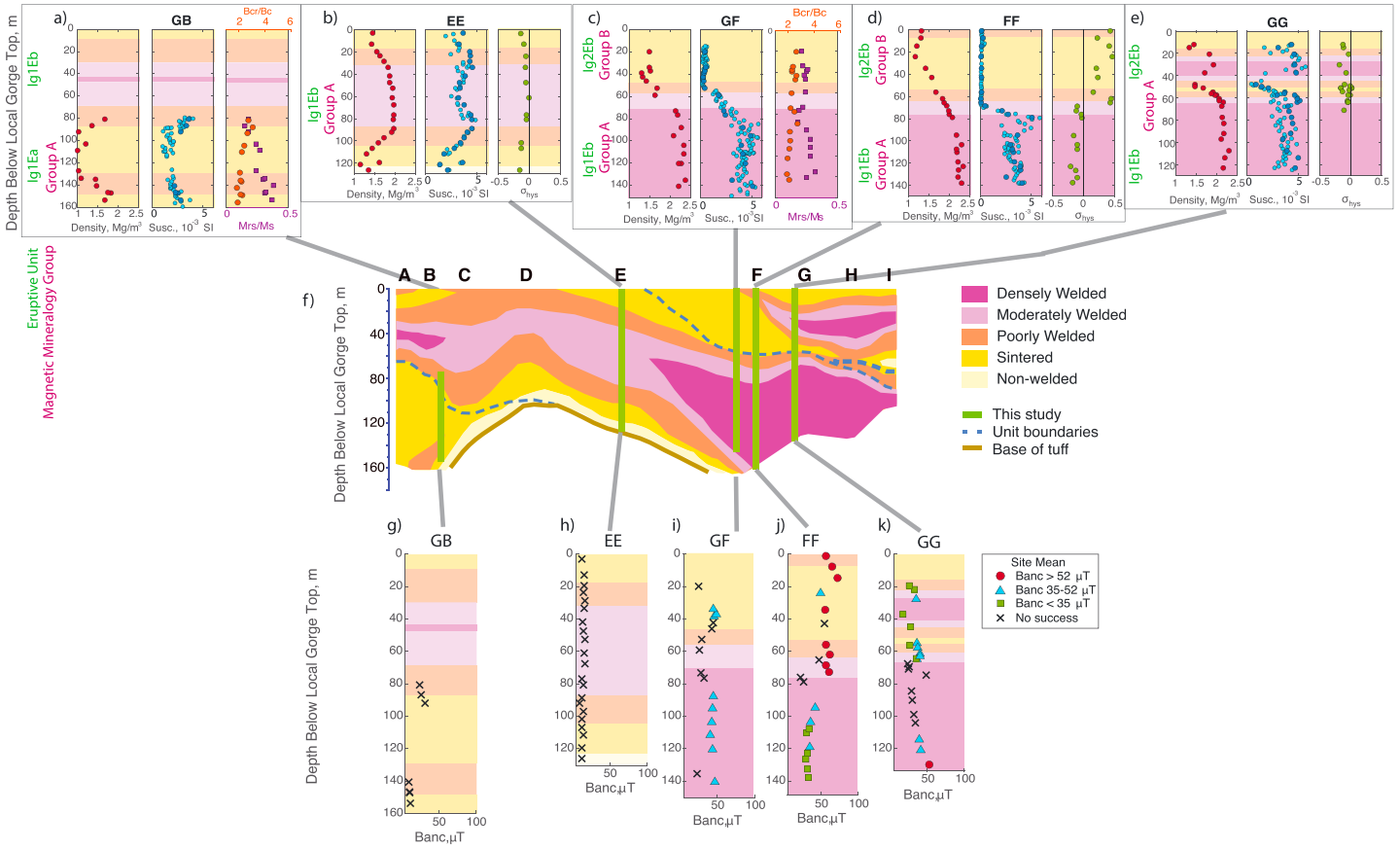

Figure 10. Summary of welding, density, magnetic properties, and B_{anc} estimates as functions of stratigraphic depth. (a–e) Density, magnetic susceptibility, and σ_{hys} for each section. (f) Profile of degree of welding of the Bishop Tuff along the Owens River gorge. Modified from Wilson and Hildreth (2003). (g–k) Paleointensity results divided into subgroups: Type 1 $B_{anc} < 35$ μT (red circle), Type 2 $B_{anc} = 35–52$ μT (blue triangle), and Type 3 $B_{anc} > 50$ μT (green square). The black x indicate sites with no passing paleointensity data, plotted at the site mean of paleointensity estimated using the all temperature steps.

specimens in sections GB and EE produce low estimates of the field strength of type 1 (Figures 7a and 10g and 10h). Bowles et al. (2015) observed similar nonideal Arai plots with a large loss of NRM at low temperatures with little pTRM gain in samples from the 1912 Novarupta flow that they interpret as features of vapor-phase alteration and found that this nonideal behavior underestimated the known paleointensity value. There are no obvious rock magnetic properties that distinguish sections GB and EE from the rest of mineralogy group B, but these sections have lower densities and degrees of welding (Figure 10f). Because these sections are closer to the caldera than are sections FF and GG, they presumably were emplaced at a temperature similar to or even slightly higher than the other sections. One possibility is that the lower initial thickness of the GB and EE sections led to faster cooling and provided less time for the growth of microcrystals of low-Ti titanomagnetite. The other sections of the tuff with group B magnetic mineralogy (section GG, and the lower portions of GF and FF) produce paleointensity estimates mostly of types 1 and 2.

Mineralogy group A is found in the upper part of the GF and FF sections and displays: decreased NRM, decreased susceptibility, increased high-coercivity phase titanohematite, increased paleointensity, and increased paleointensity scatter (Table 3). Many Arai plots from this mineralogy group are hinged, the higher temperature hematite component has a steeper slope than the lower temperature magnetite component, and these fail our criteria (Figure 7e). However, the upper portion of section FF does produce some type 3 paleointensity estimates that pass our selection criteria, which are significantly higher than the bottom of section FF, GF, and GG sections (Figures 7c and 10j). The average estimate from the upper portion of section FF is 1.6 times larger and specimen estimates from each site have much larger scatter than the estimates from the lower portion. This difference cannot be explained by cooling rate; the lower part of FF has a higher degree of

Table 3
Summary of Magnetic Mineralogy Group Properties

Characteristic	Group A	Group B
Interpreted mineralogy	Titanohematite and low-Ti (titano)magnetite	Low-Ti (titano) magnetite and (titano)maghemite
Location	Upper portion of FF and GF sections	Sections EE and GG, lower portion of FF and GF sections
Coercivity	Significant high coercivity and low coercivity phases	Just lower-coercivity phases
Unblocking temperatures	~650° (high coercivity), ~540° (low coercivity)	520–580°, 600–620°
Hysteresis loops, σ_{hys}	Wasp-waisted, $\sigma_{hys} > 0$	Slightly pot-bellied, $\sigma_{hys} < 0$
Low temperature	No Morin transition	Smeared Verwey transition
Susceptibility	$0.05–0.1 \times 10^{-3}$ SI	$2–5 \times 10^{-3}$ SI

welding indicating it cooled more slowly than the upper portion. If the difference in B_{anc} estimates were due to cooling rate differences, the bottom of FF would have a higher B_{anc}.

We use independent information on the postemplacement thermal/alteration history of the tuff, which bears on the remanence, to decide where a reliable estimate of B_{anc} can be found. Our best estimate for B_{anc} comes from the densely welded bottom portions of unit Ig1Eb that was emplaced above the Curie temperature of magnetite and possibly above the Curie temperature of maghemite, and its low permeability minimized any effects from vapor-phase alteration. This section of the Bishop Tuff with density ≥ 2.0 Mg/m^3 produces an estimate of $B_{anc} = 39.6 \pm 9.9$ μT.

5. Conclusions

We find that portions of the Bishop Tuff produce high quality paleointensity estimates though with a bimodal distribution. A portion of the tuff produces significantly higher paleointensity estimates than the rest of the tuff, probably due to a chemical remanence acquired during vapor-phase alteration. We interpret the most densely-welded portions of the tuff as the most likely to have a simple TRM and to yield accurate paleofield estimates. Future paleointensity studies of similar large ignimbrites with complex thermal and alteration histories should be very specific in their documentation of the geologic material (density and alteration) and where it came from within the ash flow.

Three new stratigraphic sections of the Bishop Tuff within the Owens River show the effect of cooling and alteration history on the magnetic mineralogy in a large ignimbrite. At some sampling locations, evidence of vapor-phase alteration explains the presence of titanohematite, which likely carries a TCRM and should be avoided for paleointensity studies. Our best estimate for B_{anc} comes from the densely welded base of unit Ig1Eb, $B_{anc} = 39.6 \pm 9.9$ μT. Our study has a few implications for future magnetic studies of ignimbrites. Strict paleointensity selection criteria alone will not necessarily reject all non-thermal remanences, as suggested both theoretically and experimentally (Draeger et al., 2006; Fabian, 2009). Therefore, samples should be collected away from zones of severe hydrothermal alteration, and petrologic and rock-magnetic evidence should be used to reject non-thermal remanence.

Acknowledgments
We thank C. Sprain and R. Fu for their thoughtful reviews that helped improve the manuscript. This work was supported by National Science Foundation (NSF) grant EAR0943999. This research constituted a portion of the doctoral dissertation of MSA. The Institute for Rock Magnetism is supported by the NSF Instruments and Facilities program. The data from this study are available in the Magnetics Information Consortium (MagIC) database [https://earthref.org/MagIC/16504/224339fa-c543-477c-8ef5-38947455dc6c].

References

Bowles, J. A., Gee, J. S., Jackson, M. J., & Avery, M. S. (2015). Geomagnetic paleointensity in historical pyroclastic density currents: Testing the effects of emplacement temperature and postemplacement alteration. *Geochemistry, Geophysics, Geosystems*, *16*, 3607–3625. https://doi.org/10.1002/2015GC005910

Bowles, J. A., & Jackson, M. J. (2016). Effects of titanomagnetite reordering processes on thermal demagnetization and paleointensity experiments. *Geochemistry, Geophysics, Geosystems*, *17*, 4848–4858. https://doi.org/10.1002/2016GC006607

Bowles, J. A., Jackson, M. J., Berquo, T. S., Sølheid, P. A., & Gee, J. S. (2013). Inferred time and temperature-dependent cation ordering in natural titanomagnetites. *Nature Communications*, *4*(1), 1916. https://doi.org/10.1038/ncomms2938

Cai, S., Tauxe, L., & Cromwell, G. (2017). Paleointensity from subaerial basaltic glasses from the Second Hawaii Scientific Drilling Project (HSDP2) core and implications for possible bias in data from lava flow interiors. *Journal of Geophysical Research: Solid Earth*, *122*, 8664–8674. https://doi.org/10.1002/2017JB014683

Coe, R. S., Grommé, S., & Mankinen, E. A. (1978). Geomagnetic paleointensities from radiocarbon-dated lava flows on Hawaii and the question of the Pacific nondipole low. *Journal of Geophysical Research*, *83*(B4), 1740–1756. https://doi.org/10.1029/JB083iB04p01740

Cromwell, G., Trusdell, F., Tauxe, L., Staudigel, H., & Ron, H. (2017). Holocene paleointensity of the island of Hawai'i from glassy volcanics. *Geochemistry, Geophysics, Geosystems*. https://doi.org/10.1002/2017GC006927

Davies, C. J., & Constable, C. G. (2014). Insights from geodynamo simulations into long-term geomagnetic field behaviour. *Earth and Planetary Science Letters*, *411*, 20–26. https://doi.org/10.1016/j.epsl.2014.11.045

Draeger, U., Prévot, M., Poidras, T., & Riisager, J. (2006). Single-domain chemical, thermochemical and thermal remanences in a basaltic rock. *Geophysical Journal International*, *166*(1), 12–32. https://doi.org/10.1111/j.1365-246X.2006.02862.x

Driscoll, P. E. (2016). Simulating 2 Ga of geodynamo history. *Geophysical Research Letters*, *43*, 5680–5687. https://doi.org/10.1002/2016GL068858

Dunlop, D. J., & Özdemir, Ö. (2001). *Rock magnetism: fundamentals and frontiers* (Vol. 3, p. 62). Cambridge, UK: Cambridge University Press.

Dunlop, D. J., & Özdemir, Ö. (2015). Magnetizations in rocks and minerals. In G. Schubert (Ed.), *Treatise on Geophysics* (2nd ed., chap. 8, Vol. 5, pp. 277–336). Amsterdam, Netherlands. https://doi.org/10.1016/B978-0-444-53802-4.00102-0

Eick, P. M., & Schlinger, C. M. (1990). The use of magnetic susceptibility and its frequency dependence for delineation of a magnetic stratigraphy in ash-flow tuffs. *Geophysical Research Letters*, *17*(6), 783–786. https://doi.org/10.1029/GL017i006p00783

Ericsson, T., Krisnhamurthy, A., & Srivastava, B. K. (1986). Morin transition in Ti-substituted hematite: A Mössbauer study. *Physica Scripta*, *33*(1), 88–90. https://doi.org/10.1088/0031-8949/33/1/013

Evans, B. W., Hildreth, W., Bachmann, O., & Scaillet, B. (2016). In defense of magnetite-ilmenite thermometry in the Bishop Tuff and its implication for gradients in silicic magma reservoirs. *American Mineralogist*, *101*(2), 407–414. https://doi.org/10.2138/am- 2016-5367

Fabian, K. (2003). Some additional parameters to estimate domain state from isothermal magnetization measurements. *Earth and Planetary Science Letters*, *213*(3-4), 337–345. https://doi.org/10.1016/S0012-821X(03)00329-7

Fabian, K. (2009). Thermochemical remanence acquisition in single-domain particle ensembles: A case for possible overestimation of the geomagnetic paleointensity. *Geochemistry, Geophysics, Geosystems*, *10*, Q06Z03. https://doi.org/10.1029/2009GC002420

Fabian, K., Shcherbakov, V. P., & McEnroe, S. A. (2013). Measuring the curie temperature. *Geochemistry, Geophysics, Geosystems*, *14*, 947–961. https://doi.org/10.1029/2012gc004440

Fu, R. R., Weiss, B. P., Lima, E. A., Kehayias, P., Araujo, J. F. D. F., Glenn, D. R., et al. (2017). Evaluating the paleomagnetic potential of single zircon crystals using the Bishop Tuff. *Earth and Planetary Science Letters*, *458*, 1–13. https://doi.org/10.1016/j.epsl.2016.09.038

Gee, J. S., Tauxe, L., & Constable, C. (2008). AMSSpin: A LabVIEW program for measuring the anisotropy of magnetic susceptibility with the Kappabridge KLY-4S. *Geochemistry, Geophysics, Geosystems*, *9*, Q08Y02. https://doi.org/10.1029/2008GC001976

Gee, J. S., Yu, Y., & Bowles, J. (2010). Paleointensity estimates from ignimbrites: An evaluation of the bishop tuff. *Geochemistry, Geophysics, Geosystems*, *11*, Q03010. https://doi.org/10.1029/2009GC002834

Geissman, J. W., Newberry, N. G., & Peacor, D. R. (1983). Discrete single-domain and pseudo-single-domain titanomagnetite particles in silicic glass of an ash-flow tuff. *Canadian Journal of Earth Sciences*, *20*(2), 334–338. https://doi.org/10.1139/e83-030

Giordano, D., Nichols, A. R., & Dingwell, D. B. (2005). Glass transition temperatures of natural hydrous melts: A relationship with shear viscosity and implications for the welding process. *Journal of Volcanology and Geothermal Research*, *142*(1-2), 105–118. https://doi.org/10.1016/j.jvolgeores.2004.10.015

Grunder, A. L., Laporte, D., & Druitt, T. H. (2005). Experimental and textural investigation of welding: Effects of compaction, sintering, and vapor-phase crystallization in the rhyolitic Rattlesnake Tuff. *Journal of Volcanology and Geothermal Research*, *142*(1-2), 89–104. https://doi.org/10.1016/j.jvolgeores.2004.10.018

Halgedahl, S. L., Day, R., & Fuller, M. (1980). The effect of cooling rate on the intensity of weak-field TRM in single-domain magnetite. *Journal of Geophysical Research*, *85*(B7), 3690–3698. https://doi.org/10.1002/JB085iB07p03690

Hildreth, W. (1979). The Bishop Tuff: Evidence for the origin of compositional zonation in silicic magma chambers. *Geological Society of America Special Papers*, *180*, 43–76. https://doi.org/10.1130/SPE180-p43

Hildreth, W., & Wilson, C. J. N. (2007). Compositional zoning of the Bishop Tuff. *Journal of Petrology*, *48*(5), 951–999. https://doi.org/10.1093/petrology/egm007

Holt, E. W., & Taylor, H. P. (1998). $^{18}O/^{16}O$ mapping and hydrogeology of a short-lived (~10 years) fumarolic (>500°C) meteoric-hydrothermal event in the upper part of the 0.76 Ma Bishop Tuff outflow sheet, California. *Journal of Volcanology and Geothermal Research*, *83*(1-2), 115–139. https://doi.org/10.1016/S0377-0273(98)00014-6

Holt, E. W., & Taylor, H. P. (2001). $^{18}O/^{16}O$ studies of fossil fissure fumaroles from the Valley of Ten Thousand Smokes, Alaska. *Bulletin of Volcanology*, *63*(2-3), 151–163. https://doi.org/10.1007/s004450100131

Ickert, R. B., Mundil, R., Magee, C. W., & Mulcahy, S. R. (2015). The U–Th–Pb systematics of zircon from the Bishop Tuff: A case study in challenges to high-precision Pb/U geochronology at the millennial scale. *Geochimica et Cosmochimica Acta*, *168*, 88–110. https://doi.org/10.1016/j.gca.2015.07.018

Jackson, M. J., & Bowles, J. A. (2014). Curie temperatures of titanomagnetite in ignimbrites: Effects of emplacement temperatures, cooling rates, exsolution, and cation ordering. *Geochemistry, Geophysics, Geosystems*, *15*, 4343–4368. https://doi.org/10.1002/2014GC005527

Keith, T. E. C. (1991). Fossil and active fumaroles in the 1912 eruptive deposits, Valley of Ten Thousand Smokes, Alaska. *Journal of Volcanology and Geothermal Research*, *45*(3-4), 227–254. https://doi.org/10.1016/0377-0273(91)90061-4

Keith, T. E. C., & Muffler, L. J. P. (1978). Minerals produced during cooling and hydrothermal alteration of ash flow tuff from Yellowstone drill hole Y-5. *Journal of Volcanology and Geothermal Research*, *3*(3–4), 373–402. https://doi.org/10.1016/0377-0273(78)90044-6

Kirschvink, J. L. (1980). The least squares line and plane and the analysis of paleomagnetic data. *Geophysical Journal International*, *62*(3), 699–718. https://doi.org/10.1111/j.1365-246X.1980.tb02601.x

Lowrie, W. (1990). Identification of ferromagnetic minerals in a rock by coercivity and unblocking temperature properties. *Geophysical Research Letters*, *17*(2), 159–162. https://doi.org/10.1029/GL017i002p00159

Mark, D. F., Renne, P. R., Dymock, R. C., Smith, V. C., Simon, J. I., Morgan, L. E., et al. (2017). High-precision $^{40}Ar/^{39}Ar$ dating of Pleistocene tuffs and temporal anchoring of the Matuyama-Brunhes boundary. *Quaternary Geochronology*, *39*, 1–23. https://doi.org/10.1016/j.quageo.2017.01.002

McIntosh, W. C., Sutter, J. F., Chapin, C. E., & Kedzie, L. L. (1990). High-precision $^{40}Ar/^{39}Ar$ sanidine geochronology of ignimbrites in the Mogollon-Datil volcanic field, southwestern New Mexico. *Physics of the Earth and Planetary Interiors*, *52*(8), 584–601. https://doi.org/10.1007/BF00301210

Mochizuki, N., Maruuchi, T., Yamamoto, Y., & Shibuya, H. (2013). Multi-level consistency tests in paleointensity determinations from the welded tuffs of the Aso pyroclastic-flow deposits. *Physics of the Earth and Planetary Interiors*, *223*, 40–54. https://doi.org/10.1016/j.pepi.2013.05.001

Mullins, C. E., & Tite, M. S. (1973). Magnetic viscosity, quadrature susceptibility, and frequency dependence of susceptibility in single-domain assemblies of magnetite and maghemite. *Journal of Geophysical Research*, *78*(5), 804–809. https://doi.org/10.1029/JB078i005p00804

Özdemir, Ö., & Dunlop, D. J. (2010). Hallmarks of maghemitization in low-temperature remanence cycling of partially oxidized magnetite nanoparticles. *Journal of Geophysical Research*, *115*, B02101. https://doi.org/10.1029/2009JB006756

Özdemir, Ö., Dunlop, D. J., & Berquó, T. S. (2008). Morin transition in hematite: Size dependence and thermal hysteresis. *Geochemistry, Geophysics, Geosystems*, *9*, Q10Z01. https://doi.org/10.1029/2008GC002110

Palmer, H. C., MacDonald, W. D., Grommé, C. S., & Ellwood, B. B. (1996). Magnetic properties and emplacement of the Bishop Tuff, California. *Bulletin of Volcanology*, *58*(2-3), 101–116. https://doi.org/10.1007/s004450050129

Paterson, G. A., Tauxe, L., Biggin, A. J., Shaar, R., & Jonestrask, L. C. (2014). On improving the selection of Thellier-type paleointensity data. *Geochemistry, Geophysics, Geosystems*, *15*, 1180–1192. https://doi.org/10.1002/2013GC005135

Perrin, M., Alva-Valdivia, L. M., Lopez-Martinez, M., Rosas-Elguera, J., Benammi, M., Gonzalez-Rangel, J. A., & Camps, P. (2013). Palaeomagnetism of the upper volcanic supergroup, southern part of the Sierra Madre Occidental, Mexico. *Geophysical Journal International*, *193*(3), 1250–1264. https://doi.org/10.1093/gji/ggt079

Petrovsky, E., & Kapicka, A. (2006). On determination of the Curie point from thermomagnetic curves. *Journal of Geophysical Research*, *111*, B12S27. https://doi.org/10.1029/2006JB004507

Reynolds, R. L. (1977). Paleomagnetism of welded tuffs of the Yellowstone group. *Journal of Geophysical Research*, *82*(26), 3677–3693. https://doi.org/10.1029/JB082i026p03677

Riehle, J. R. (1973). Calculated compaction profiles of rhyolitic ash-flow tuffs. *Geological Society of America Bulletin*, *84*(7), 2193–2216. https://doi.org/10.1130/0016-7606(1973)84<2193:CCPORA>2.0.CO;2

Riehle, J. R., Miller, T. F., & Bailey, R. A. (1995). Cooling, degassing and compaction of rhyolitic ash flow tuffs: A computational model. *Bulletin of Volcanology*, *57*(5), 319–336. https://doi.org/10.1007/BF00301291

Roberts, A. P., Cui, Y., & Verosub, K. L. (1995). Wasp-waisted hysteresis loops: Mineral magnetic characteristics and discrimination of components in mixed magnetic systems. *Journal of Geophysical Research*, *100*(B9), 17,909–17,924. https://doi.org/10.1029/95JB00672

Rosenbaum, J. G. (1993). Magnetic grain-size variations through an ash flow sheet: Influence on magnetic properties and implications for cooling history. *Journal of Geophysical Research*, *98*(B7), 11,715–11,727. https://doi.org/10.1029/93JB00355

Sarna-Wojcicki, A. M., Pringle, M. S., & Wijbrans, J. (2000). New $^{40}Ar/^{39}Ar$ age of the Bishop Tuff from multiple sites and sediment rate calibration for the Matuyama-Brunhes boundary. *Journal of Geophysical Research*, *105*(B9), 21,431–21,443. https://doi.org/10.1029/2000JB900901

Schlinger, C. M., Griscom, D., Papaefthymiou, G. C., & Veblen, D. R. (1988). The nature of magnetic single domains in volcanic glasses of the KBS Tuff. *Journal of Geophysical Research*, *93*(B8), 9137–9156. https://doi.org/10.1029/JB093iB08p09137

Schlinger, C. M., Rosenbaum, J. G., & Veblen, D. R. (1988). Fe-oxide microcrystals in welded tuff from southern Nevada: Origin of remanence carriers by precipitation in volcanic glass. *Geology*, *16*(6), 556–559. https://doi.org/10.1130/0091-7613(1988)016<0556:FOMIWT>2.3.CO;2

Schlinger, C. M., Veblen, D. R., & Rosenbaum, J. G. (1991). Magnetism and magnetic mineralogy of ash flow tuffs from Yucca Mountain, Nevada. *Journal of Geophysical Research*, *96*(B4), 6035–6052. https://doi.org/10.1029/90JB02653

Selkin, P., & Tauxe, L. (2000). Long-term variations in palaeointensity. *Philosophical Transactions of the Royal Society of London A: Mathematical, Physical and Engineering Sciences*, *358*(1768), 1065–1088. https://doi.org/10.1098/rsta.2000.0574

Senderov, E., Dogan, A. U., & Navrotsky, A. (1993). Nonstoichiometry of magnetite-ulvospinel solid-solutions quenched from 1300° C. *American Mineralogist*, *78*(5–6), 565–573.

Shaar, R., & Tauxe, L. (2013). Thellier GUI: An integrated tool for analyzing paleointensity data from Thellier-type experiments. *Geochemistry, Geophysics, Geosystems*, *14*, 677–692. https://doi.org/10.1002/ggge.20062

Sheridan, E. (1970). Fuarmolic mounds and ridges of the Bishop Tuff, California. *Geological Society of America Bulletin*, *81*(3), 851–868. https://doi.org/10.1130/00167606(1970)81[851:FMAROT]2.0.CO;2

Sheridan, E., & Wang, Y. (2005). Cooling and welding history of the Bishop Tuff in Adobe Valley and Chidago Canyon, California. *Journal of Volcanology and Geothermal Research*, *142*(1-2), 119–144. https://doi.org/10.1016/j.jvolgeores.2004.10.016

Smirnov, A. V., Tarduno, J. A., Kulakov, E. V., McEnroe, S. A., & Bono, R. K. (2016). Palaeointensity, core thermal conductivity and the unknown age of the inner core. *Geophysical Journal International*, *205*(2), 1190–1195. https://doi.org/10.1093/gji/ggw080

Stoner, E. C., & Wohlfarth, E. P. (1948). A mechanism of magnetic hysteresis in heterogeneous alloys. *Philosophical Transactions of the Royal Society of London A*, *240*(826), 599–642. https://doi.org/10.1098/rsta.1948.0007

Tauxe, L., Mullender, T. A. T., & Pick, T. (1996). Potbellies, wasp-waists, and superparamagnetism in magnetic hysteresis. *Journal of Geophysical Research*, *101*(B1), 571–583. https://doi.org/10.1029/95JB03041

Tauxe, L., Shaar, R., Jonestrask, L., Swanson-Hysell, N. L., Minnett, R., Koppers, A. A., et al. (2016). PmagPy: Software package for paleomagnetic data analysis and a bridge to the Magnetics Information Consortium (MagIC) database. *Geochemistry, Geophysics, Geosystems*, *17*, 2450–2463. https://doi.org/10.1002/2016GC006307

Tauxe, L., & Staudigel, H. (2004). Strength of the geomagnetic field in the Cretaceous Normal Superchron: New data from submarine basaltic glass of the Troodos Ophiolite. *Geochemistry, Geophysics, Geosystems*, *5*, Q02H06. https://doi.org/10.1029/2003GC000635

van der Bogaard, P., & Schirnick, C. (1995). $^{40}Ar/^{39}Ar$ laser probe ages of Bishop Tuff quartz phenocrysts substantiate long-lived silicic magma chamber at Long Valley, United States. *Geology*, *23*(8), 759–762. https://doi.org/10.1130/0091-7613(1995)023<0759:AALPAO>2.3.CO;2

Vaniman, D. (2006). Tuff mineralogy. In G. Heiken (Ed.), *Tuffs—Their properties, uses, hydrology, and resources* (Vol. 408, pp. 11–15). Boulder, CO: Geological Society of America. https://doi.org/10.1130/SPE408

Wilson, C. J. N., & Hildreth, W. (1997). The bishop tuff: New insights from eruptive stratigraphy. *The Journal of Geology*, *105*(4), 407–440. https://doi.org/10.1086/515937

Wilson, C. N., & Hildreth, W. (2003). Assembling an ignimbrite: Mechanical and thermal building blocks in the Bishop Tuff, California. *The Journal of Geology*, *111*(6), 653–670. https://doi.org/10.1086/378335

Worm, H.-U., & Jackson, M. (1999). The superparamagnetism of Yucca Mountain Tuff. *Journal of Geophysical Research*, *104*(B11), 25,415–25,425. https://doi.org/10.1029/1999JB900285

Wright, H. M. N., Lesti, C., Cas, R. A. F., Porreca, M., Viramonte, J. G., Folkes, C. B., & Giordano, G. (2011). Columnar jointing in vapor-phase-altered, non-welded Cerro Galn Ignimbrite, Paycuqui, Argentina. *Bulletin of Volcanology*, *73*(10), 1567–1582. https://doi.org/10.1007/s00445-011-0524-6

Yu, Y., Tauxe, L., & Genevey, A. (2004). Toward an optimal geomagnetic field intensity determination technique. *Geochemistry, Geophysics, Geosystems*, *5*, Q02H07. https://doi.org/10.1029/2003GC000630